Anharmonic Properties of the Vibrational Two-Qubit System

Yingying Gu
Marquette University

ANHARMONIC PROPERTIES OF THE VIBRATIONAL TWO-QUBIT SYSTEM

by

Yingying Gu

A Thesis submitted to the Faculty of the Graduate School,
Marquette University,
in Partial Fulfillment of the Requirements for
the Degree of Master of Science

Milwaukee, Wisconsin

August 2011

ABSTRACT
ANHARMONIC PROPERTIES OF THE VIBRATIONAL TWO-QUBIT SYSTEM

Yingying Gu

Marquette University, 2011

My thesis focuses on theoretical studies in the molecular quantum computing with vibrational qubits. We studied how the molecular vibrational properties affect the fidelity of the logic gates. Our approach is to encode states of the quantum information register into the vibrational eigenstates of a molecule and use the shaped laser pulse (femtosecond, infrared) to control the vibrational state-to-state transition. By using the Optimal Control Theory to shape a femtosecond laser and numerical propagation of laser-driven vibrational wave packets, we analyzed how the vibrational properties of a two-qubit system affect the accuracy of the quantum gates and how to effectively control the vibrational state-to-state transitions. From these studies, we found the anharmonicities are very important for the control of the vibrational state-to-state transitions and an intricate interplay between the frequencies and anharmonicities in the two-qubit system leads to the occurrence of resonances between different transitions in the vibrational manifold. Such resonances cause "leakage" of population into other vibrational states and hinder the control. From theoretical analysis of resonances, we formulate several criteria for selection of molecule for implementation of the vibrational two-qubit system. These criteria can help experimentalists to choose the best molecules to achieve accurate qubit transformations in the experiment.

ACKNOWLEDGMENTS

Yingying Gu

Foremost, I would like to express my sincere gratitude to my advisor Dr. Dmitri Babikov for the continuous support of my study and research, for his patience, motivation, enthusiasm and immense knowledge. His guidance helped me in all the time of research and writing of this thesis. I appreciate all his contributions of time and ideas to make my experience stimulating in Quantum Physics.

Beside my advisor, I would like to thank the rest of my thesis committee: Dr. Michael D. Ryan and Dr. Qadir Timerghazin for their encouragement, insightful comments. My sincere thanks also go to Dr. James R. Kincaid and Mr. Vaughn Ausman for helping and supporting me.

The members of Dr. Babikov's group have contributed immensely to me. The group has been a source of friendships, good advice and collaborations. I would like to acknowledge our past and present group members: postdoc Meiyu Zhao and Evgeny Vetoshkin; and graduate students Lei Wang, Leidi Jiang and Xiang Cheng.

Lastly, I would like to thank my family for all their love and encouragement. For my parents who love and support me in all my pursuits. Thank you.

TABLE OF CONTENTS

LIST OF TABLES

LIST OF FIGURES

CHAPTER 1: INTRODUCTION

In recent years several different approaches to implement quantum information bits (qubits) by using molecular vibrational eigenstates have been proposed and explored theoretically[1-43], indicating favorable paths to experimental implementation. The main idea is to encode states of the quantum information register into the vibrational eigenstates of a molecule and use the shaped laser pulses (femtosecond, infrared) to manipulate these states and to process quantum information efficiently by applying the quantum logics gates. Such laser pulses should be optimized for the desired state-to-state transitions, which can be achieved in the experiment by using the feedback control techniques and the evolutionary algorithms. In the simplest approach to molecular qubits the ground vibrational state and the first excited vibrational state of the molecule can be employed to represent the states $|0\rangle$ and $|1\rangle$ of the qubit. An arbitrary state of the qubit is represented by the vibrational wave packet -- coherent superposition of vibrational eigenstates, and can be driven by the laser pulse (coherently) towards any desired final state. A non-linear gas-phase molecule has $3N$-6 normal vibrational modes. Different qubits can be encoded into different normal vibration modes of a molecule, suggesting an approach to scaling.

The vibrational qubits were first suggested by Vivie-Riedle and co-workers[1-4]. They considered theoretically a two-qubit quantum register encoded into two IR-active normal vibration modes of acetylene molecule, C_2H_2. The reduced dimensionality model was used for the wave packet propagation. The optimal control theory was employed in order to predict shapes of the pulses for major quantum gates.

Their choice of acetylene was mostly due to historic reasons: in the past this group studied spectroscopy and control of this molecule and had the potential energy surface and the dipole-moment function for acetylene available.

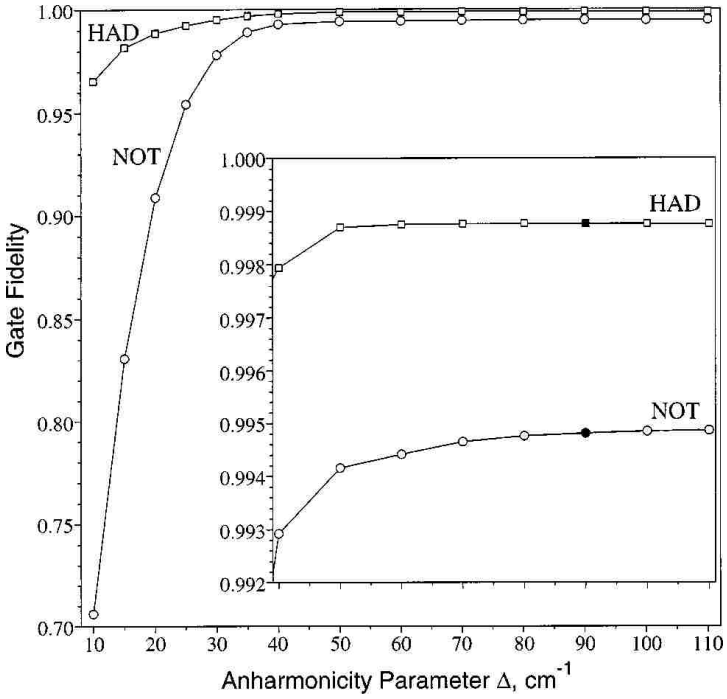

Fig. 1.1 Fidelities of the gates NOT and Hadamard as a function of anharmonicity parameter of the model system. The insert is used to show the same two curves in detail in the region of high fidelity plateau. Filled symbols describe the case of natural OH diatomic. [Babikov, **2004**, 7582]

The question on how the molecular characteristics affect the fidelity of gate operations and how to choose the best possible molecule for implementation of the vibrational qubits has been addressed by Babikov.[5] He first began with OH molecule as a vibrational one-qubit system and obtained highly accurate optimal pulses for several one-qubit gates. Then, using the analytic model of the Morse oscillator function, he theoretically "tuned" the anharmonicity parameter of the molecule, Δ, through a board range of values, $10\ cm^{-1} \leq \Delta \leq 110\ cm^{-1}$ (note that vibrations of the

natural "true" OH are quite anharmonic, Δ = 90 cm^{-1}). Babikov discovered clear correlation between anharmonicity of the molecule and accuracy of the quantum gates. Results from his paper are presented in Fig. 1.1. It was found that fidelity of gates increases quickly as anharmonicity is increased. The high fidelity plateau was observed in the region Δ > 50 cm^{-1} (see Fig. 1.1). The conclusion was that large anharmonicty is a dominant factor in achieving high fidelity of gates in the vibrational qubits. Indeed, it is quite clear that the state-to-state transitions in a purely harmonic oscillator cannot be controlled selectively because all vibrational states are equidistant and the transition frequencies are equal. If the transition $|0\rangle \rightarrow |1\rangle$ is induced, the transitions $|1\rangle \rightarrow |2\rangle$, $|2\rangle \rightarrow |3\rangle$, etc., will also follow, because transitions between these states all occur at the same harmonic frequency. So anharmonicities are very important for the control of vibrational state-to-state transitions. It was concluded that choosing a candidate for experimental implementation of vibrational qubits one should focus on molecules with high vibrational anharmonicities.

The search for a suitable candidate molecule for quantum computation has begun and several new candidates were proposed, including $C_{10}H_8$,[12] I_2,[13] $MnBr(CO)_5$,[16] NH_3,[18] CO,[35,37] NO,[36] HF,[40] LiCs,[42] gas phase D_3O^+,[38] Na_2^+,[41] MgH^+ [43] and an experimental for Li_2[10]. Fundamental prospects of vibrational state-to-state transitions were studied by Sibert III, Gruebele and Weidinger.[21,22] Grollub and co-workers analyzed the effects of molecular characteristics on the structure of the global quantum gates and found that the coupling in multimode systems is also important.[19,20]

The goal of my research was to extend the ideas of Babikov and co-workers [5,12] onto the two-qubit case. It was found that such extension is not straightforward. Obviously, in a two-qubit system, two intramode vibrational anharmonicities are needed (Δ_1 and Δ_2) in order to control each qubit individually. Equally important is the intermode anharmonicity (Δ_{12}) responsible for coupling of the two modes. Surprisingly, it was found that simply taking all three anharmonicity parameters large (for example $\Delta_1 = \Delta_2 = \Delta_{12} = 100$ cm^{-1}) does not give a controllable two-qubit system! Analysis showed that an intricate interplay between the frequencies and anharmonicities in the two-qubit system leads to the occurrence of resonances between different transitions in the vibrational manifold. Such resonances cause "leakage" of population into other vibrational states and hinder the control. A systematic analysis of this effect was the main goal of my work.

Theoretical analysis of resonances in a two-qubit system is presented in Chapter 2. In Chapter 3 we review the Optimal Control Theory as applied to pulse shaping and describe the model used in this work to describe the laser control of molecular vibrations. In Chapter 4 the results of extensive numerical experiments are presented. Chapter 5 is dedicated to detailed analysis of the control mechanisms. The criteria for selection of molecule for implementation of the vibrational two-qubit system are formulated in Chapter 6.

CHAPTER 2: THEORETICAL APPROACH

2.1 Vibrational Two-qubit System

One way to implement a vibrational two-qubit system is to encode the two qubits into two different vibrational normal modes of a polyatomic molecule. Figure 2.1 below shows a Hilbert space spanned by two normal vibration modes and a 2×2 space of a two-qubit system encoded into the ground state $|00\rangle$, first excited state in each mode $|01\rangle$ and $|10\rangle$, and the combination state $|11\rangle$. This is one natural choice, but other choices are also possible.

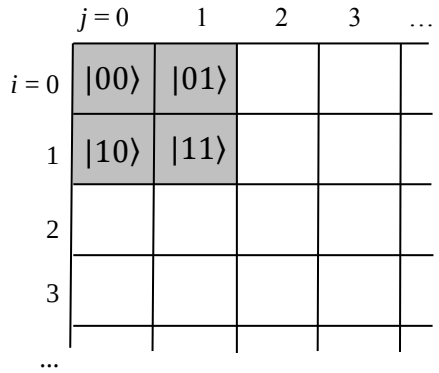

Fig. 2.1 Hilbert space for two-qubit system

In the two-qubit case the role of molecular anharmonicities is even more pronounced. From the Introduction section, it is clear that the intramode anharmonicities are needed in order to ensure that each qubit can be individually controlled, but equally important is the intermode anharmonicity (coupling) which is needed to ensure that , for example, the $|00\rangle \rightarrow |01\rangle$ and the $|10\rangle \rightarrow |11\rangle$ transitions

occur at different frequencies and can be controlled selectively. The 2D Dunham's expansion (in atomic units) contains these three parameters:

$$E_{ij} = \omega_1 (i+\tfrac{1}{2}) - \Delta_1 (i+\tfrac{1}{2})^2 + \omega_2 (j+\tfrac{1}{2}) - \Delta_2 (j+\tfrac{1}{2})^2 - \Delta_{12} (i+\tfrac{1}{2})(j+\tfrac{1}{2}) , \qquad (2.1.1)$$

where $\boldsymbol{\omega_1}$ and $\boldsymbol{\omega_2}$ correspond to harmonic frequencies, $\boldsymbol{\Delta_1}$ and $\boldsymbol{\Delta_2}$ are intramode anharmonicity parameters, and $\boldsymbol{\Delta_{12}}$ describes the intermode anharmonicity or the coupling effect. Although this idea is intuitively simple, the increase in complexity of the spectrum carries some nonobvious caveats. It was found in Ref. [12] showed that the interplay between frequencies and anharmonicities in Eq. (2.1.1) can lead to occurrence of groups of resonances between different transitions in the vibrational manifold which we are trying to control. Such resonances cause "leakage" of population from the 2×2 qubit space into the upper vibrational states, which hinders the control. Accurate control of the state-to-state transition is impossible (or at least very difficult) in a molecule with vibrational characteristics close to such resonance. In this work, we study this effect in order to avoid choosing an inappropriate candidate molecule for vibrational quantum computation. We restrict our considerations to the 2D Dunham Hamiltonian, Eq. (2.1.1), and study its suitability for quantum computation. In the regime of low vibrational excitation, specific to good vibrational qubits, this approximation is expected to be reasonably accurate for a broad variety of molecules.

We focus on small polyatomic molecules and consider two suitable normal modes that can be used to represent a vibrational subspace of two qubits (see Fig. 2.1) unaffected by decoherence on a time scale of optimal control (picoseconds). The ground vibrational state, the first excited state in each mode, and the combination

state are chosen to represent $|00\rangle$, $|01\rangle$, $|10\rangle$ and $|11\rangle$ states of the two-qubit system, respectively. According to standard convention, the first qubit is the control qubit and the second qubit is the target qubit. In this work we study in detail a one-qubit gate NOT (in Section 2.2) and a two-qubit gate CNOT (in Section 2.3) in this system.

We assume that the spectrum of the two-dimensional vibrational manifold in Fig. 2.1 is described reasonably well by the Dunham's expansion, Eq. (2.1.1). This approximation is usual in spectroscopy and is often used to fit long progressions of vibrational states[30]. Here we focus on the low vibrational excitation regime, when only a few lower vibrational states are populated and this formula is expected to work especially well. Note that Eq. (2.1.1) has five parameters plus the overall energy shift (not included in Eq. (2.1.1) for simplicity). This means that the values of energies of any six states can be fitted by this expression exactly. Those can be, for example, four states of the 2×2 qubit-space plus two overtone states $|02\rangle$ and $|20\rangle$. If this approach is chosen, the other upper states will be reproduced approximately but, again, this approximation is good for the low vibrational excitation regime.

As discussed in the Introduction, accurate transformations of the qubit states are difficult if the frequency of the transition we are trying to control is similar to the frequency of some other state-to-state transition, which can be a transition to an upper vibrational state (outside of the qubit space) or another transition between the qubit states. First consider the transformation of the target (second) qubit only. Frequency of the $|00\rangle \leftrightarrow |01\rangle$ can be close to frequency of the following transitions: $|01\rangle \leftrightarrow |02\rangle$, $|11\rangle \leftrightarrow |12\rangle$ and $|10\rangle \leftrightarrow |11\rangle$. All these transitions change state of the second qubit by one quantum only and, in general, their frequencies are close to each other. It is easy

to image a situation when two of these transitions are in exact resonance so that the control is impossible. This effect is important only when the resonant transitions involve states that are energetically close to each other. For this reason we did not include transitions $|20\rangle \leftrightarrow |21\rangle$ and $|21\rangle \leftrightarrow |22\rangle$ into the list; these transitions include states that are energetically further from the states $|00\rangle$ and $|01\rangle$. (They are outside of the 2×2 qubit space. We will discuss these and other similar cases in more detail at Sec. 2.2 and 2.3)

2.2 Analysis of Resonance Patterns for One-qubit Gates

The one-qubit gate is NOT on the second qubit, or unconditional NOT,

$$\begin{aligned} &\mathrm{NOT}|00\rangle \to |01\rangle, \\ &\mathrm{NOT}|01\rangle \to |00\rangle, \\ &\mathrm{NOT}|10\rangle \to |11\rangle, \\ &\mathrm{NOT}|11\rangle \to |10\rangle. \end{aligned} \qquad (2.2.1)$$

This gate NOT flips the state of the target qubit irrespectively to the state of the control qubit.

The spectrum in Eq. (2.1.1) has a special property. If we require that the $|00\rangle \leftrightarrow |01\rangle$ transition is in resonance with the $|01\rangle \leftrightarrow |02\rangle$ transition, the resonance will also occur between any pair of transitions conforming to notations $|i, j\rangle \leftrightarrow |i, j+1\rangle$ and $|i, j+1\rangle \leftrightarrow |i, j+2\rangle$. We call this feature *a pattern of resonances*. If the proximity of states discussed in the previous paragraph is taken into account, it appears that the number of such patterns is very limited, just those four shown in Fig.

2.2. In this figure, arrows of same color are used to indicate resonant transitions. The following four expressions describe the resonance patterns shown in Fig. 2.2, frames (a)−(d), respectively:

$$|i, j\rangle \leftrightarrow |i, j+1\rangle \quad \text{and} \quad |i, j+1\rangle \leftrightarrow |i, j+2\rangle, \tag{2.2.2a}$$

$$|i, j\rangle \leftrightarrow |i, j+1\rangle \quad \text{and} \quad |i+1, j+1\rangle \leftrightarrow |i+1, j+2\rangle, \tag{2.2.2b}$$

$$|i, j\rangle \leftrightarrow |i, j+1\rangle \quad \text{and} \quad |i+1, j\rangle \leftrightarrow |i+1, j+1\rangle, \tag{2.2.2c}$$

$$|i, j\rangle \leftrightarrow |i, j+1\rangle \quad \text{and} \quad |i-1, j+1\rangle \leftrightarrow |i-1, j+2\rangle. \tag{2.2.2d}$$

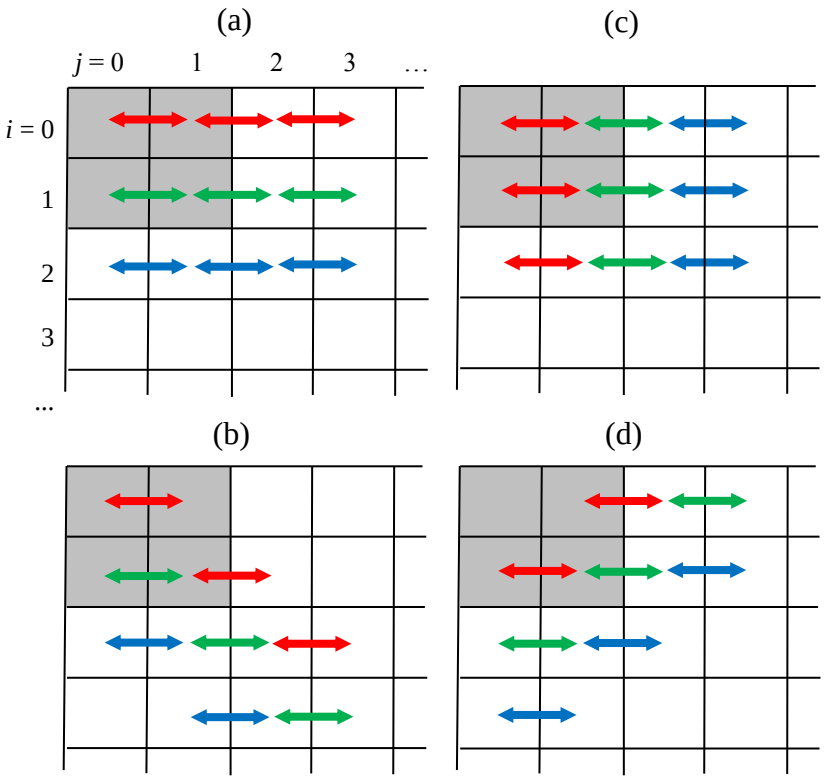

Fig. 2.2 Patterns of resonance for the target qubit mode. Arrows of same color show resonant transitions.

We can use Eq. (2.1.1) to express frequencies for transitions in Eqs. (2.2.2a−d). Equating the resonant frequencies and using some algebra we can derive analytic expressions that represent conditions for observing a given pattern of resonances of Fig. 2.2, frames (a)−(d), respectively:

$$\Delta_2 = 0, \tag{2.2.3a}$$

$$2\Delta_2 + \Delta_{12} = 0, \tag{2.2.3b}$$

$$\Delta_{12} = 0, \tag{2.2.3c}$$

$$2\Delta_2 - \Delta_{12} = 0. \tag{2.2.3d}$$

Derivations for these expressions (2.2.3a−d) are given in Appendix A. Note that both frequencies, ω_1 and ω_2 have been canceled out completely. Equations (2.2.3a−d) contain only the coefficient of anharmonicity for the target qubit, Δ_2, and the inter-mode anharmonicity coefficient, Δ_{12}. This result, again, underlines the fundamental role of anharmonicity in the control. This also means that the patterns of Eqs. (2.2.3a−d) are practically important for any two modes of any molecule, irrespectively to the values of frequencies of two modes, ω_1 and ω_2.

In the work of Ref. [12], Babikov studied a resonance between $|01\rangle \leftrightarrow |02\rangle$ and $|20\rangle \leftrightarrow |21\rangle$ transitions which confirms to a pattern,

$$|i, j\rangle \leftrightarrow |i, j+1\rangle \text{ and } |i+2, j-1\rangle \leftrightarrow |i+2, j\rangle. \tag{2.2.2e}$$

The negative effect of this resonance was observed in numerical optimal control calculations[12] but was shown to be quite small (~1% drop of the gate fidelity) due to

significant separation of the states involved in these transitions. A similar resonance may also occur between the $|00\rangle \leftrightarrow |01\rangle$ and $|21\rangle \leftrightarrow |22\rangle$ transitions that confirm to a pattern,

$$|i, j\rangle \leftrightarrow |i, j+1\rangle \text{ and } |i+2, j-1\rangle \leftrightarrow |i+2, j\rangle . \tag{2.2.2f}$$

For the same reason (large separation of states) such resonances are expected to play only a minor role and are not studied in detail in this work.

2.3 Analysis of Resonance Patterns for Two-qubit Gates

The two-qubit gate CNOT (conditional NOT) flips the state of the target qubit (second qubit) only if the control qubit (first qubit) is in state $|1\rangle$:

$$\begin{aligned} &\text{CNOT}|00\rangle \rightarrow |00\rangle, \\ &\text{CNOT}|01\rangle \rightarrow |01\rangle, \\ &\text{CNOT}|10\rangle \rightarrow |11\rangle, \\ &\text{CNOT}|11\rangle \rightarrow |10\rangle . \end{aligned} \tag{2.3.1}$$

Considerations similar to those in the previous section, but with the control qubit involved, lead to the patterns of resonances shown schematically in Fig. 2.3. Note that in all the cases shown in this figure a transition in the target qubit ($|00\rangle \leftrightarrow |01\rangle$ or $|10\rangle \leftrightarrow |11\rangle$) is in resonance with a transition along the control mode. In the cases shown in frames (a)−(c) of Fig. 2.3 both resonant transitions involve only states of the 2×2 qubit space, while in the cases shown in frames (d)−(f) of Fig. 2.3 one of the resonant transitions lead to the states outside of the 2×2 qubit space.

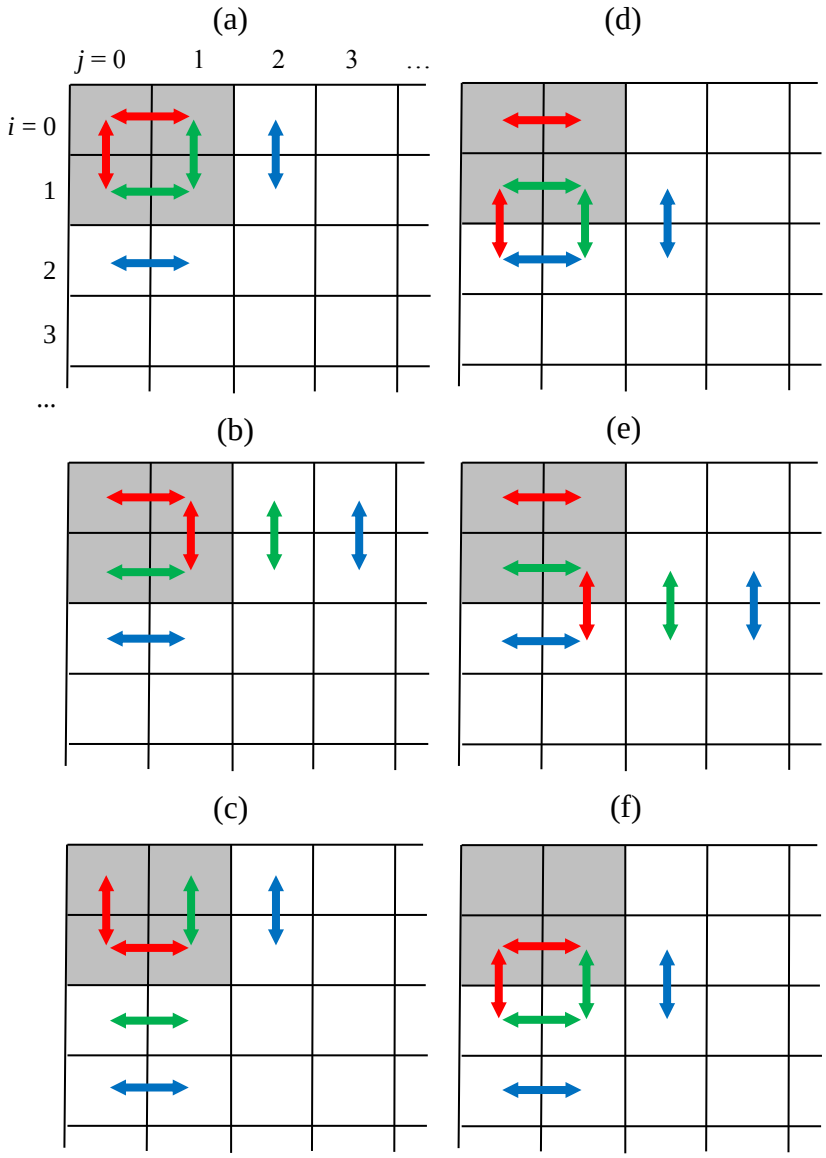

Fig. 2.3 Patterns of resonances between the control and the target qubit modes. Arrows of same color show resonant transitions.

The following expressions describe the resonance patterns shown in Fig. 2.3, frames (a)−(f), respectively:

$$|i, j\rangle \leftrightarrow |i, j+1\rangle \text{ and } |i, j\rangle \leftrightarrow |i+1, j\rangle, \tag{2.3.2a}$$

$$|i, j\rangle \leftrightarrow |i, j+1\rangle \text{ and } |i, j+1\rangle \leftrightarrow |i+1, j+1\rangle, \tag{2.3.2b}$$

$$|i+1, j\rangle \leftrightarrow |i+1, j+1\rangle \text{ and } |i, j\rangle \leftrightarrow |i+1, j\rangle, \tag{2.3.2c}$$

$$|i, j\rangle \leftrightarrow |i, j+1\rangle \text{ and } |i+1, j\rangle \leftrightarrow |i+2, j\rangle, \tag{2.3.2d}$$

$$|i, j\rangle \leftrightarrow |i, j+1\rangle \text{ and } |i+1, j+1\rangle \leftrightarrow |i+2, j+1\rangle, \tag{2.3.2e}$$

$$|i+1, j\rangle \leftrightarrow |i+1, j+1\rangle \text{ and } |i+1, j\rangle \leftrightarrow |i+2, j\rangle. \tag{2.3.2f}$$

Using Eq. (2.1.1) to express frequencies for transitions of Eqs. (2.3.2a)−(2.3.2f), equating the resonant frequencies and using some algebra we can derive analytic expressions that represent conditions for observing a given pattern of resonances in Fig. 2.3, frames (a)−(f), respectively:

$$2\Delta_1 - 2\Delta_2 = \omega_1 - \omega_2, \tag{2.3.3a}$$

$$2\Delta_1 - 2\Delta_2 + \Delta_{12} = \omega_1 - \omega_2, \tag{2.3.3b}$$

$$2\Delta_1 - 2\Delta_2 - \Delta_{12} = \omega_1 - \omega_2, \tag{2.3.3c}$$

$$4\Delta_1 - 2\Delta_2 = \omega_1 - \omega_2, \tag{2.3.3d}$$

$$4\Delta_1 - 2\Delta_2 + \Delta_{12} = \omega_1 - \omega_2, \tag{2.3.3e}$$

$$4\Delta_1 - 2\Delta_2 - \Delta_{12} = \omega_1 - \omega_2. \tag{2.3.3f}$$

Derivations of expressions (2.3.3a)−(2.3.3f) are given in Appendix B. All these equations, unlike Eqs. (2.2.3a)−(2.2.3d), contain the anharmonicity parameter of the control qubit, Δ_1, as well as the frequency difference between the two vibrational modes, $\omega_1 - \omega_2$. This last property means that such resonance patterns are also quite

general and the conclusions obtained for one system transferable to other systems with the same value of $\omega_1 - \omega_2$, even if the frequencies are different.

2.4 Low Fidelity Planes

All the equations (2.2.3a)−(2.2.3d) and (2.3.3a)−(2.3.3f) have a general analytic form $a\Delta_1 + b\Delta_2 + c\Delta_{12} = \text{constant}$, which can be represented as a plane in the three-dimensional anharmonicity parameter space: Δ_1, Δ_2 and Δ_{12}. We call such planes the *low fidelity planes* because the points in their vicinity describe systems that are hard to control, which results in low accuracy (or fidelity) of gates. Figure 2.4 (a) shows low fidelity planes given by Eqs. (2.2.3a)−(2.2.3d). For convenience, the planes of Eqs. (2.2.3a), (2.2.3b), (2.2.3d) and (2.2.3c) are labeled as $a^{(0)}$, $a^{(-)}$, $a^{(+)}$ and $b^{(0)}$, respectively. All four planes cross each other along the Δ_1-axis which makes this picture symmetric with respect to the sign change in any variable: Δ_1, Δ_2 or Δ_{12}.

Recall that most often anharmonicity in a molecule is positive, but examples are known when the vibrational spectrum exhibits negative anharmonicity. For this reason the range of anharmonicities in Fig. 2.4 is chosen from -10 cm^{-1} to $+40$ cm^{-1} along each axis. It does not matter in which of the eight quadrants of the ($\Delta_1, \Delta_2, \Delta_{12}$)-space our system is, the four planes of Fig. 2.4 (a) will have the same structure and effect. From analysis of this figure, one can immediately conclude that the region in the vicinity of Δ_1-axis, where both Δ_2 and Δ_{12} are small, is the most problematic. Any point in this region describes a system in which the control will be negatively affected by several patterns of resonances.

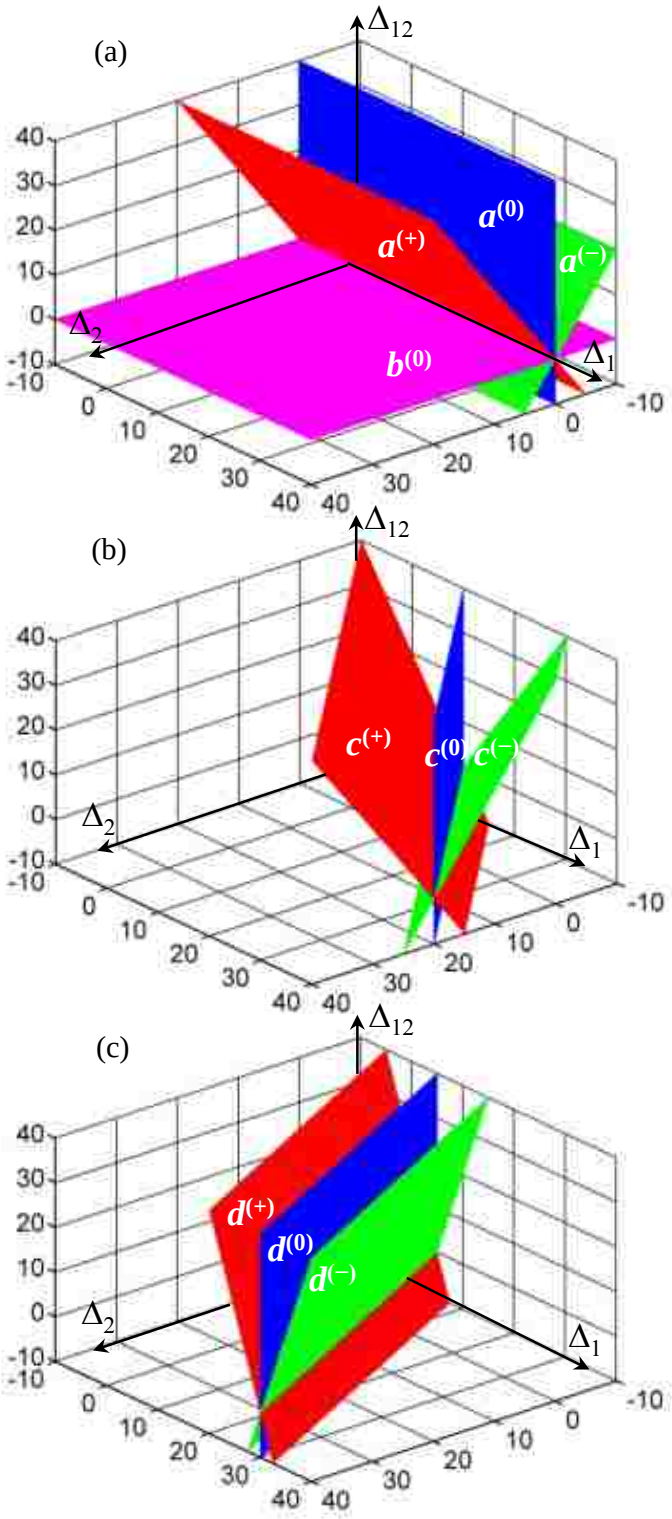

Fig. 2.4 Low fidelity planes in the $(\Delta_1, \Delta_2, \Delta_{12})$-space. (a) Four planes $a^{(0)}$, $a^{(+)}$, $a^{(-)}$ and $b^{(0)}$ given by Eqs. (2.2.3a–d); (b) Three planes $c^{(0)}$, $c^{(+)}$ and $c^{(-)}$ given by Eqs. (2.3.3a–c); (c) Three planes $d^{(0)}$, $d^{(+)}$ and $d^{(-)}$ given by Eqs. (2.3.3d–f);

Note that positions of planes in Fig. 2.4 (a) do not depend on the values of frequencies ω_1 and ω_2 simply because Eqs. (2.2.3a)−(2.2.3d) do not contain frequencies. Thus, these four low fidelity planes are the most general and should be important for broad variety of molecules. In contrast, the planes given by Eqs. (2.3.3a)−(2.3.3f) contain frequencies and their location in the $(\Delta_1, \Delta_2, \Delta_{12})$-space will be different for different molecules. For the numerical calculations of this work (Chapter 4), we choose $\omega_1 - \omega_2$ = 40 cm^{-1}. This choice is arbitrary, but it allows us to observe and study all six planes of Eqs. (2.3.3a)−(2.3.3f) in the vicinity of the origin, where the values of anharmonicity parameters are not very large, which corresponds to naturally occurring molecules. With this choice of $\omega_1 - \omega_2$, the three planes given by Eqs. (2.3.3a)−(2.3.3c) are shown in Fig. 2.4 (b), while the three planes given by Eqs. (2.3.3d)−(2.3.3f) are shown in Fig. 2.4 (c). The three planes in each set, either Fig. 2.4 (b) or Fig. 2.4 (c), lie close to each other and form a well-defined region of low fidelity in the $(\Delta_1, \Delta_2, \Delta_{12})$-space. For convenience, the planes of a set of Eqs. (2.3.3a), (2.3.3b) and (2.3.3c) are labeled as $c^{(0)}$, $c^{(+)}$ and $c^{(-)}$ respectively (see Fig. 2.4(b)). The planes of a set of Eqs. (2.3.3d), (2.3.3e) and (2.3.3f) are labeled as $d^{(0)}$, $d^{(+)}$ and $d^{(-)}$ respectively (see Fig. 2.4 (c)). Three planes in each set cross along the line that belongs to the $\Delta_{12} = 0$ plane.

The overall picture is rather complicated because all ten low fidelity planes, Eqs. (2.2.3a)−(2.2.3d) and (2.3.3a)−(2.3.3f), are simultaneously present in the $(\Delta_1, \Delta_2, \Delta_{12})$-space. They are presented in three different frames of Fig. 2.4 only for the reason of clarity. However, the breakdown into the three groups (Fig. 2.4 (a), (b) and (c)) make sense, because the patterns of resonances in each group have similar

features and the planes in each group are located close to each other and move together through the $(\Delta_1, \Delta_2, \Delta_{12})$-space when the value of $\omega_1 - \omega_2$ is changed.

CHAPTER 3: THEORETICAL TOOLS

In this approach to quantum computation, the gates are applied to qubits using the shaped laser pulses to induce the desired state-to-state transition and suppress the interfering ones. The optimal control theory (OCT) is used to theoretically design the shapes of such pulses.

3.1 Time-dependent Schrödinger Equation

The evolution of the vibrational wave function satisfies the time-dependent Schrodinger equation:

$$i\frac{\partial}{\partial t}\psi(Q_1,Q_2,t)=\hat{H}\psi(Q_1,Q_2,t) \tag{3.1.1}$$

where

$$\hat{H}=\hat{H}_0-\varepsilon(t)\cdot\mu(Q_1,Q_2) \tag{3.1.2}$$

is a 2D Hamiltonian operator.

$$\hat{H}_0\equiv-\frac{1}{2m_1}\frac{\partial^2}{\partial Q_1^2}-\frac{1}{2m_2}\frac{\partial^2}{\partial Q_2^2}+V(Q_1,Q_2)\,. \tag{3.1.3}$$

Here Q_1 and Q_2 represent the two normal modes coordinates, $\hat{H}_0$ is molecular Hamiltonian in the absence of external field, $\varepsilon(t)$ is the time-dependent electrical field of the shaped laser pulse, and $\mu(Q_1,Q_2)$ is the dipole moment function of the molecule. From the work of Ref. [5], it is known that under the control of an

optimized laser pulse on a vibrational qubit just few vibrational eigenstates of $\hat{H}_0$ acquire a non-negligible population. In such case, it is convenient to expand the wave function in a basis set of vibrational eigenstates,

$$\psi(Q_1, Q_2, t) = \sum_{ij} c_{ij}(t) \left| \varphi_{ij}(Q_1, Q_2) \right\rangle e^{-iE_{ij}t} , \tag{3.1.4}$$

where the energy eigenvalues E_{ij} and eigenfunctions φ_{ij} of $\hat{H}_0$ are labeled by two quantum numbers *i* and *j* that represent the number of vibrational quanta in each normal mode. In practice, it is enough to include only five states in each mode $0 \le i \le 4$ and $0 \le j \le 4$, so there are a total of 25 states in the sum of Eq. (3.1.4). Substituting this expansion into the Schrodinger Equation (3.1.1), and projecting the result into the vibrational eigenstates $e^{+iE_{kl}t} \left\langle \varphi_{kl}(Q_1, Q_2) \right|$, we can obtain the following equations for the probability amplitudes (Derivations are given in Appendix C):

$$\dot{c}_{ij}(t) = i\varepsilon(t) \sum_{kl} c_{kl}(t) M_{kl,ij} e^{-i(E_{ij} - E_{kl})t} , \tag{3.1.5}$$

where $M_{ij,kl}$ are elements of the standard dipole moment matrix. These equations show that the time evolution of the probability amplitudes is driven by the magnitude of the electric field $\varepsilon(t)$, the values of corresponding elements of the dipole moment matrix $M_{ij,kl}$, and the energy separation of the corresponding vibrational states, $E_{kl} - E_{ij}$. In order to solve the Eq. (3.1.5), we need to know the spectrum of energy eigenvalues E_{ij} and all elements of the dipole moment matrix $M_{ij,kl}$.

3.2 Energy Spectrum and Dipole Moment Matrix

Propagation of the time-dependent Schrödinger equation for evolution of vibrational wave packet driven by the laser field requires only the knowledge of energies of the system and of elements of its dipole moment matrix. We assume that energy spectrum is described by the Dunham's expression, Eq. (2.1.1), which is an approximation used routinely in spectroscopy. The dipole moment function in the vicinity of the equilibrium point is approximated by linear terms in the Taylor series expansion, which leads to a simplified structure of the dipole moment matrix. The dipole moment matrix can be computed as

$$M_{kl,ij} = \left\langle \varphi_{kl}(Q_1,Q_2) \right| \mu(Q_1,Q_2) \left| \varphi_{ij}(Q_1,Q_2) \right\rangle_{Q_1,Q_2}, \tag{3.2.1}$$

where the indices i and k label the initial states, j and l label the final states. The dipole moment μ is a function of two coordinates Q_1 and Q_2, but in the vicinity of the equilibrium point the higher order terms of Taylor expansion can be neglected and the dipole moment function can be expressed as

$$\mu(Q_1,Q_2) \approx \mu_0 + \mu_1' Q_1 + \mu_2' Q_2 \ . \tag{3.2.2}$$

Since we exploit the regime of low vibrational excitation, we can approximate the two-dimensional vibrational eigenstates in Eq. (3.2.1) by the product of harmonic oscillator function for the normal modes,

$$\left|\varphi_{ij}(Q_1,Q_2)\right\rangle \approx \left|\varphi_i(Q_1)\varphi_j(Q_2)\right\rangle = \left|i,j\right\rangle \tag{3.2.3}$$

We use harmonic approximation only in the calculation of the dipole moment matrix in Eq. (3.2.1). The spectrum of states is essentially anharmonic. Substitution of Eqs. (3.2.2) and (3.2.3) into Eq. (3.2.1), allows obtaining the following analytic expression for elements of the dipole moment matrix:

$$\begin{aligned} M_{kl,ij} &= \mu_0 \langle k|i\rangle_{Q_1} \langle l|j\rangle_{Q_2} + \mu_1' \langle k|Q_1|i\rangle \langle l|j\rangle_{Q_2} + \mu_2' \langle k|i\rangle_{Q_1} \langle l|Q_2|j\rangle_{Q_2} \\ &= \mu_0 \delta_{k,i}\delta_{l,j} + \frac{\mu_1'}{\sqrt{2m_1\omega_1}}(\sqrt{k}\delta_{k,i+1} + \sqrt{k+1}\delta_{k,i-1})\delta_{l,j} \\ &+ \frac{\mu_2'}{\sqrt{2m_2\omega_2}}(\sqrt{l}\delta_{l,j+1} + \sqrt{l+1}\delta_{l,j-1})\delta_{k,i} \end{aligned} \tag{3.2.4}$$

where m_1 and m_2 are effective masses of the two normal modes, μ_1' and μ_2' are derivatives of the dipole moment function along the two normal modes, $\delta_{l,j}$ is the usual Kronecker symbol, and the indices *i* and *k* (*j* and *l*) are used to label initial and final vibrational states of the first (second) normal mode.

We have to admit that some molecules exhibit complicated potential energy surfaces and dipole moment functions, which potentially could lead to a non-negligible deviation of their spectrum from that of Eq. (2.1.1) and to a structure of their dipole moment matrix more complicated than that of Eq. (3.2.4). Such rare cases do require special treatment that can be quite complicated, especially if accurate quantitative results are needed (e.g., for comparison with experiment). For those special cases the approximate framework used here may not be sufficient. In this work, however, we are interested in qualitative theoretical analysis and confirmation of the ideas outlined in Chapter 2. For this purpose, in the regime of low vibrational excitation specific to our problem, the approximations of Eq. (2.1.1) and Eq. (3.2.4) hold and our treatment can be applied to a broad variety of molecules.

3.3 Optimal Control Theory

We use the Optimal Control Theory (OCT) to theoretically shape the laser pulses for the desired transformations of states of the vibrational qubits. The purpose of OCT is to find the laser pulse $\varepsilon(t)$ which maximizes the transfer of population from a given initial state ϕ_i to a chosen final state ϕ_f. The two-qubit gates of Eq. (2.2.1) or Eq. (2.3.1) involve four transitions of interest. Suitable optimization is achieved by maximizing the objective functional where the sum over all the four transitions is introduced:

$$K = \sum_{k=1}^{4} \left(\left| \left\langle \psi_i^{[k]} \middle| \phi_f^{[k]} \right\rangle \right|^2 \right) - \int_0^T \alpha \mid \varepsilon(t) \mid^2 dt$$
$$- \sum_{k=1}^{4} 2\,\mathrm{Re} \left\{ \left\langle \psi_i^{[k]} \middle| \phi_f^{[k]} \right\rangle \int_0^T \left\langle \psi_f^{[k]}(t) \middle| i\hat{H} + \frac{\partial}{\partial t} \middle| \psi_i^{[k]}(t) \right\rangle dt \right\}. \qquad (3.3.1)$$

Here the index *k* labels the four transitions of interest. The $\psi_i^{[k]}(t)$, $k = \{1, 2, 3, 4\}$, are the laser-driven time-dependent wave functions and $\psi_f^{[k]}(t)$ is the backward driven wave function. The $\varepsilon(t)$ is the universal gate field which drives a wave function $\psi_i^{[k]}(t)$ from the initial states $\psi_i^{[k]}(t=0) = \phi_i^{[k]}$ to the final state $\psi_i^{[k]}(t=T) = \phi_f^{[k]}$. For example, for the gate NOT we set, $\phi_i^{[1]} = |00\rangle$, $\phi_f^{[1]} = |01\rangle$, $\phi_i^{[2]} = |01\rangle$, $\phi_f^{[2]} = |00\rangle$, $\phi_i^{[3]} = |10\rangle$, $\phi_f^{[3]} = |11\rangle$, $\phi_i^{[4]} = |11\rangle$, $\phi_f^{[4]} = |10\rangle$, according to Eq. (2.2.1). The function α is a penalty function:

$$\alpha = \alpha(t) = \frac{\alpha_0}{s(t)}\ , \qquad (3.3.2)$$

where α_0 is a constant penalty factor, $s(t)$ plays a role of a smooth envelope of the pulse:

$$s(t) = \sin^2(\pi t / T). \tag{3.3.3}$$

The approach is to maximize the functional Eq. (3.3.1) with respect to variations in nine functions: $\psi_i^{[k]}(t)$, $\psi_f^{[k]}(t)$, k = {1, 2, 3, 4}, and $\varepsilon(t)$. Applying variations of $\psi_f^{[1]}(t)$, $\psi_f^{[2]}(t)$, $\psi_f^{[3]}(t)$ and $\psi_f^{[4]}(t)$ to the functional (3.3.1) we obtain in each case

$$i\hbar \frac{\partial}{\partial t}\psi_i^{[k]}(t) = [H_0 - \mu\varepsilon(t)]\psi_i^{[k]}(t) \ , \ \ \psi_i^{[k]}(0) = \phi_i^{[k]}, \ k = \{1,2,3,4\}. \tag{3.3.4}$$

These are four time-dependent Schrödinger equations for the molecule-light interaction to be propagated forward in time, each one with its own initial condition $\phi_i^{[k]}$. Next, variations of $\psi_i^{[1]}(t)$, $\psi_i^{[2]}(t)$, $\psi_i^{[3]}(t)$, $\psi_i^{[4]}(t)$ in the functional (3.3.1) give

$$i\hbar \frac{\partial}{\partial t}\psi_f^{[k]}(t) = [H_0 - \mu\varepsilon(t)]\psi_f^{[k]}(t) \ , \ \ \psi_f^{[k]}(T) = \phi_f^{[k]}, \ k = \{1,2,3,4\}. \tag{3.3.5}$$

These are four time-dependent Schrödinger equations for the molecule-light interaction to be propagated backward in time, each one with its own target state $\phi_f^{[k]}$ as a boundary condition. Finally, the variation in $\varepsilon(t)$ gives

$$\varepsilon(t) = -\frac{s(t)}{\hbar\alpha_0}\,\mathrm{Im}\sum_{k=1}^{4}\left\langle \psi_i^{[k]}(t)\middle|\psi_f^{[k]}(t)\right\rangle\left\langle \psi_f^{[k]}(t)\middle|\mu\middle|\psi_i^{[k]}(t)\right\rangle, \tag{3.3.6}$$

where the sum is over the four transitions of interest. We note that the eight Schrödinger equations (3.3.4) and (3.3.5) are coupled only through the field equation (3.3.6).

The coupled Eqs. (3.3.4), (3.3.5) and (3.3.6) can be solved numerically using an iterative method.[7,8] Iterations start with some reasonable initial guess filed pulse $\varepsilon(t)$ and, at first, only Eq. (3.3.5) are propagated backward in time to determine an initial approximation to $\psi_f^{[k]}(t)$, $k = \{1, 2, 3, 4\}$. Then the coupled Eqs. (3.3.4) and (3.3.6) are propagated forward in time using $\psi_f^{[k]}(t)$ from the previous step when computing the field according to Eq. (3.3.6). This gives the initial approximation to $\psi_i^{[k]}(t)$, $k = \{1, 2, 3, 4\}$, which is now used in Eq. (3.3.6) to propagate backward in time with the coupled Eqs. (3.3.5) and (3.3.6). The iterative procedure continues in this way, and $\varepsilon(t)$ is improved in each iteration until the desired convergence is achieved.

During the iterative processing of solving Eqs. (3.3.4), (3.3.5) and (3.3.6), we can analyze the laser-driven wave functions $\psi^{[k]}$ after each propagation step by projecting them into their corresponding wave functions $\phi^{[k]}$. So the backward propagated wave functions $\psi_f^{[k]}$ are projected onto the corresponding initial qubit states $\phi_i^{[k]}$, while the forward propagated wave functions $\psi_i^{[k]}$ are projected onto the corresponding final qubit states $\phi_f^{[k]}$:

$$P_f^k = \left|\left\langle \phi_i^{[k]} \,|\, \psi_f^{[k]}(t=0)\right\rangle\right|^2,\ k = \{1,2,3,4\}, \tag{3.3.7}$$

$$P_i^k = \left|\left\langle \phi_f^{[k]} \,|\, \psi_i^{[k]}(t=T)\right\rangle\right|^2,\ k = \{1,2,3,4\}. \tag{3.3.8}$$

The four values $P_f^{[k]}$ and $P_i^{[k]}$, $k = \{1, 2, 3, 4\}$, reflect the accuracy or fidelity of the gate pulse. They can also be used to determine the convergence of iterations. So after

each iteration, we will evaluate the average of $P_f^{[k]}$ (backward propagation) over four transition,

$$F = \langle P \rangle = \frac{1}{4}\sum_{k=1}^{4} \left| \langle \phi_i^{[k]} \mid \psi_f^{[k]}(t=0) \rangle \right|^2 \tag{3.3.9}$$

and the average of $P_i^{[k]}$ (forward propagation) over four transitions,

$$F = \langle P \rangle = \frac{1}{4}\sum_{k=1}^{4} \left| \langle \phi_f^{[k]} \mid \psi_f^{[k]}(t=T) \rangle \right|^2 . \tag{3.3.10}$$

We will terminate the iteration after the desired convergence is achieved.

CHAPTER 4: NUMERICAL RESULTS

In this Chapter, in order to test the theoretical predictions of Chapter 2, we carried out numerical optimization of laser pulses for a large number of systems with different values of anharmonicity parameters (i.e., for different points in the (Δ_1, Δ_2, Δ_{12})-space of anharmonicity parameters in Fig. 2.4). For each such point we optimized the laser pulse for a given quantum gate and determined the fidelity (accuracy) of the qubit transformations.

We carried out a large number of independent OCT calculations. In a series of such computational "experiments" we varied the values of three anharmonicity parameters in Eq. (2.1.1) in the range from 5 cm^{-1} to 40 cm^{-1} with a 5 cm^{-1} step, which made up a 8 × 8 × 8 grid of points in ($\Delta_1, \Delta_2, \Delta_{12}$)-space, 512 points total. Such a grid covers a very broad variety of systems. Each case was studied independently. The values of frequencies were kept fixed at $\omega_1 = 620$ cm^{-1} and $\omega_2 = 580$ cm^{-1}, so the frequency difference was $\omega_1 - \omega_2 = 40$ cm^{-1}, as in Fig. 2.4. The choice in mid-infrared was for generality. Other parameters in Eq. (3.2.4) were chosen as follows: $m_1 = 1.0$ amu and $m_2 = 1.2$ amu, $\mu_1' = \mu_2' = 0.4$ a.u. ~ 1.0167 D/Bohr, which correspond to strong infrared absorbers. The target time (pulse duration) was T = 2 ps, the number of forward-backward iterations was 600. The penalty factor was α=0.1 which allowed us to keep the field amplitude in the optimized pulses below 0.001 a.u. ~ 5.2 kV/cm. Laser pulses for the gates NOT and CNOT were optimized independently. The results, gate fidelities, are presented in Fig. 4.1 for the gate NOT and in Fig. 4.4 for the gate CNOT (two views of the data cube are given). Red color

shows points where the fidelity of the gate is close to one (accurate control can be achieved in 2 ps) while the blue color corresponds to the fidelity close to one half (no control).

4.1 Gate NOT and the Low Fidelity Planes

Analysis of the 3D data cube in Fig. 4.1 shows that it contains five distinct regions (labeled as A, B, C, D and E) separated by the low fidelity planes (see Fig. 2.4). The main region, A, where the value of gate fidelity reaches 0.992, is located in the range of large values of Δ_2. Comparing Fig. 4.1 with Fig. 2.4 one can conclude that this part of the data cube is the most remote from all the low fidelity planes, which we believe is the fundamental reason for the high fidelity of gates. Indeed, the closest low fidelity planes are $a^{(+)}$ and $d^{(+)}$ and they both are far from this region of the $(\Delta_1, \Delta_2, \Delta_{12})$-space (see Fig. 2.4). Note that the "horizontal" plane $b^{(0)}$ has no effect on fidelity of the unconditional gate NOT (this property will be discussed in detail below). The second, smaller region of high fidelity, B, is tightly fit between planes $c^{(+)}$ and $d^{(-)}$ in Fig. 2.4. As a result, the value of fidelity here is not very high; it only reaches 0.968. Other smaller regions of even somewhat lower fidelity are the region C found between the planes $c^{(0)}$ and $c^{(+)}$, the region D found behind the plane $c^{(-)}$, and the region E behind the plane $a^{(+)}$, see Fig. 4.1.

The main feature of the entire data cube is, perhaps, the low fidelity layer that separates two high fidelity regions, A and B. This layer is formed by the group of three planes $d^{(0)}$, $d^{(+)}$ and $d^{(-)}$ (dotted lines in Fig. 4.1), which are so close to each other that the $(\Delta_1, \Delta_2, \Delta_{12})$-space between them contains no points of high fidelity.

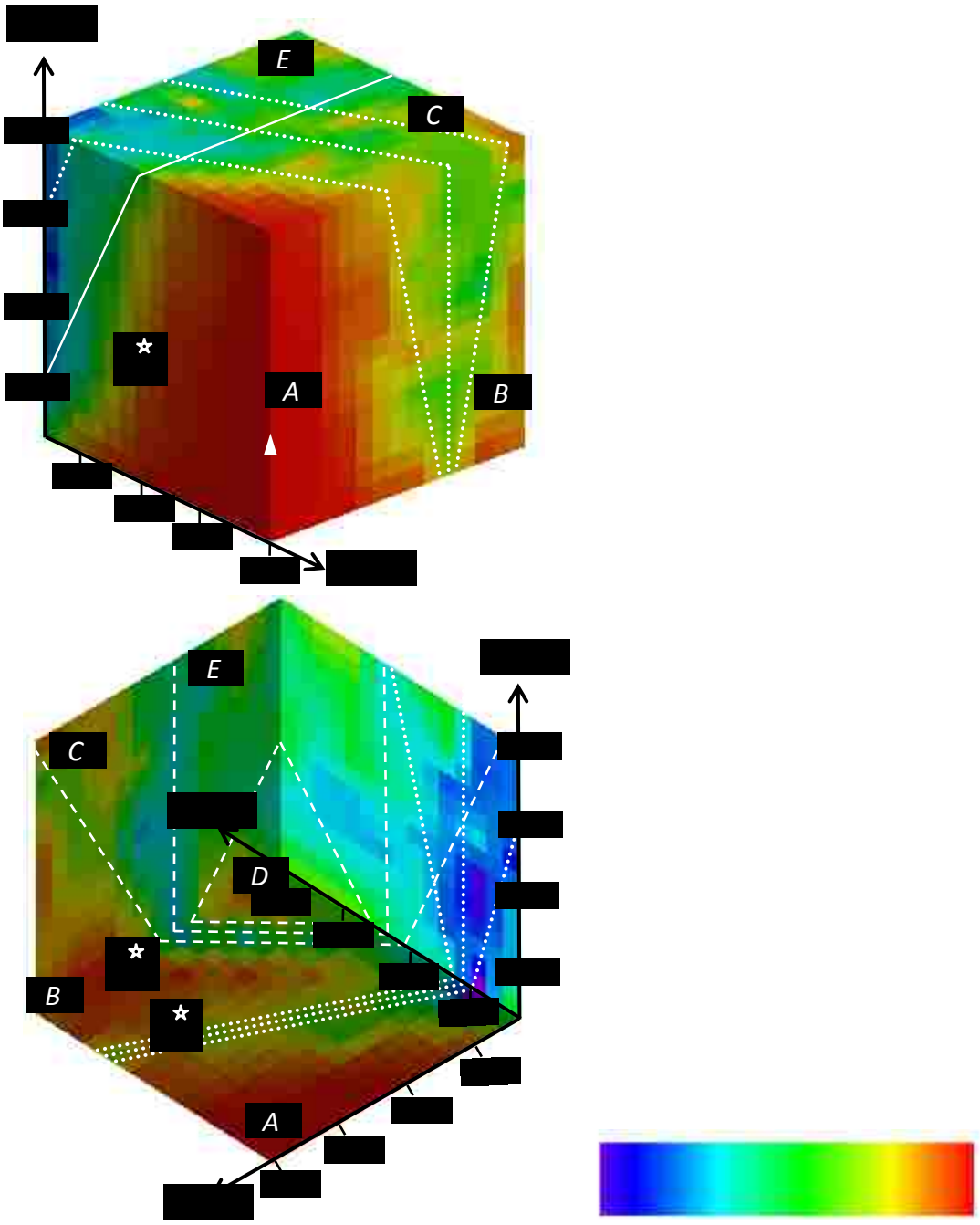

Fig. 4.1 Fidelity of optimized gate NOT in the $(\Delta_1, \Delta_2, \Delta_{12})$-space. The two different views of the same data cube are given. Red color indicates the fidelity close to 1 (highest); blue color indicates fidelity close to 0.5 (lowest). Low fidelity planes here are indicated by the white lines: solid-plane corresponding to Fig. 2.4 (a); dashed-plane corresponding to Fig. 2.4 (b); dotted-planes corresponding to Fig. 2.4 (c). Letters A, B, C, D and E indicate high fidelity regions. White triangle shows the highest fidelity point. Starts show the sample points which will be discussed in Chapter 5.

Note that, the fidelity is always low in the range of small values of Δ_2 due to proximity of the "vertical" plane $a^{(0)}$, which is just outside of the cube ($\Delta_2 = 0$). The effect of plane $a^{(+)}$ is seen very clearly in the Fig. 4.1 (a) (solid line). The effect of three planes $c^{(0)}$, $c^{(+)}$ and $c^{(-)}$ is seen very clearly in Fig. 4.1 (b) (dashed lines); they separate smaller high fidelity regions B, C and D.

Δ_1 (cm^{-1})	Δ_2 (cm^{-1})	Δ_{12} (cm^{-1})	Fidelity
5	35	5	0.9909
5	40	5	0.9917
10	40	5	0.9909
5	40	10	0.9912
10	40	10	0.9906
5	***40***	***15***	***0.9921***
10	40	15	0.9913
5	40	20	0.9919
10	40	20	0.9909
5	40	25	0.9914
5	40	30	0.9916

Table 4.1 High fidelity points in the region A of the data cube for gate NOT (see Fig. 4.1). The highest fidelity point is $(\Delta_1, \Delta_2, \Delta_{12})$ = (5, 40, 15) cm^{-1}.

In the high fidelity region A of the data cube for the gate NOT, there are several points where the fidelity is above 0.99. They are collected in Table 4.1. We can see that all these points have a large value of Δ_2 and a small value of Δ_1. The maximum value of fidelity in our calculations is 0.9921. The corresponding point is located at $(\Delta_1, \Delta_2, \Delta_{12})$ = (5, 40, 15) cm^{-1}. It is labeled by white triangle in Fig. 4.1. In vicinity of this point, the fidelity is high, exceeding the value of 0.99.

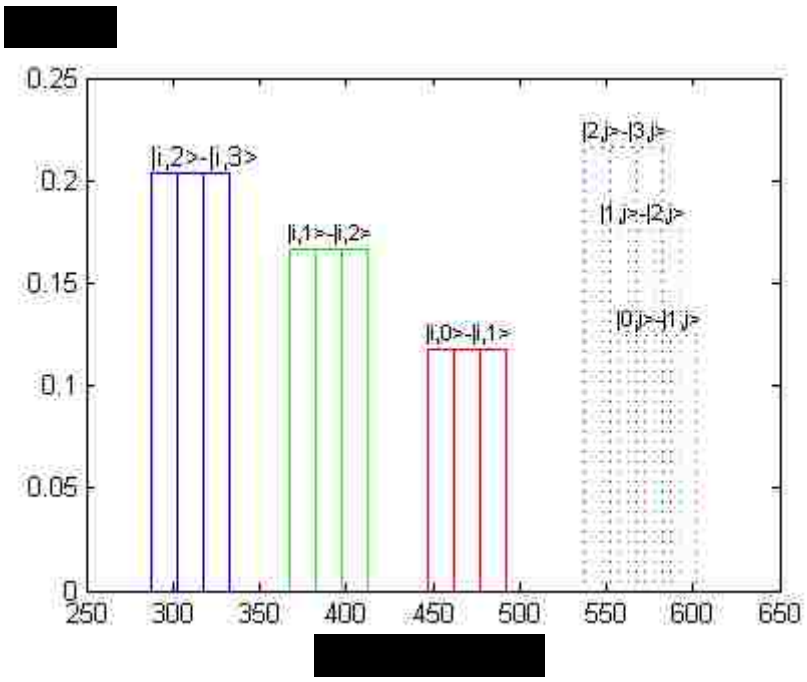

Fig. 4.2 Transition frequency diagram for the gate NOT in the two-qubit system described by ($\Delta_1, \Delta_2, \Delta_{12}$) = (5, 40, 15) cm^{-1}. None of frequencies are in resonance.

The transition frequency diagram for this point is shown in Fig. 4.2. On this diagram, a set of vertical lines represents the state-to-state transition frequencies in the spectrum of the system. The solid lines in Fig. 4.2 are used for the second (target) mode while the dotted lines are used for the first (control) mode. For example, the group of the blue solid lines, which is located closest to the left in Fig. 4.2, corresponds to frequencies of the $|i,2\rangle \rightarrow |i,3\rangle$ transition with i = {0, 1, 2, 3}, while the group of the blue dot lines corresponds to frequencies of the $|2, j\rangle \rightarrow |3, j\rangle$ transitions with j = {0, 1, 2, 3}. The vertical axis in Fig. 4.2 shows the value of the dipole moment matrix elements for these transitions. From this diagram, we can see that there is a large separation of frequencies for the transitions in the second mode, and no resonance frequencies in the entire spectrums. This behavior is controlled mostly

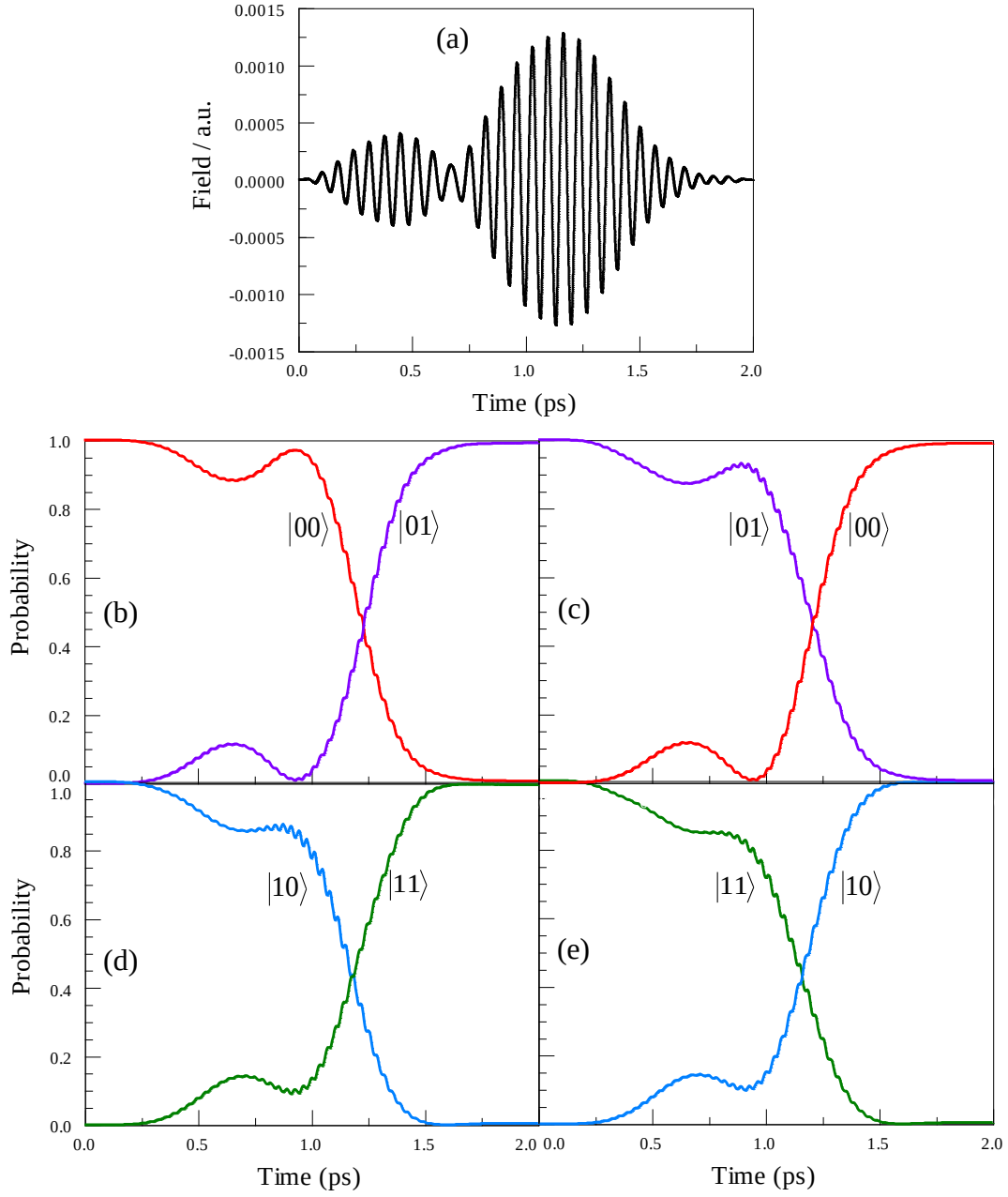

Fig. 4.3 Numerical results for the gate NOT in the two-qubit system described by $(\Delta_1, \Delta_2, \Delta_{12})$ = (5, 40, 15) cm^{-1}. (a) Optimized 2 ps laser pulse; [(b)-(e)] Evolution of the state populations during the pulse for state-to-state transitions given by Eq. (2.2.1).

(b) Transformation NOT $|00\rangle \rightarrow |01\rangle$ (c) Transformation NOT $|01\rangle \rightarrow |00\rangle$

(d) Transformation NOT $|10\rangle \rightarrow |11\rangle$ (e) Transformation NOT $|11\rangle \rightarrow |10\rangle$

by the anharmonicity parameter Δ_2. Conclusion is that a large separation of different groups of solid lines and no resonant frequencies in the spectrums of system leads to a very high fidelity of gates.

The optimized pulse for this highest fidelity point is shown Fig. 4.3 (a). The time evolution of populations of the qubit states during this pulse is shown in Fig. 4.3 (b-e) for four transitions of Eq. (2.2.1). The optimized pulse has two subpulses. The first smaller subpulse only transfers small population and the second sub-pulse completes transformation of the qubit states. Four transitions of Figure 4.6 (b-e) exhibit the decrease/increase of the probability during the pulse. The population transfer is basically direct from the initial state to the final state with a negligible population of upper vibrational states.

4.2 Gate CNOT and the Low Fidelity Planes

Analysis of the data cube for the two-qubit gate CNOT (Fig. 4.4) shows that the main difference is the presence of the horizontal low fidelity plane $b^{(0)}$. Effect of this plane is seen very clearly in Fig. 4.4. Plane $b^{(0)}$ itself is just outside the data cube ($\Delta_{12} = 0$), but fidelity of the gate CNOT drops everywhere in the region of small values of Δ_{12} due to proximity of this plane. As a result, the high fidelity region A in Fig. 4.4 is smaller than in Fig. 4.1. Due to the same effect, fidelity in the region B of Fig. 4.4 drops down to 0.946, while the region D practically disappears.

In the highest fidelity region A of the data cube for the gate CNOT, there are several points where the fidelity is above 0.99. They are collected in Table 4.2. We can see that all these points show a large value of Δ_2 and a small value of Δ_1. The

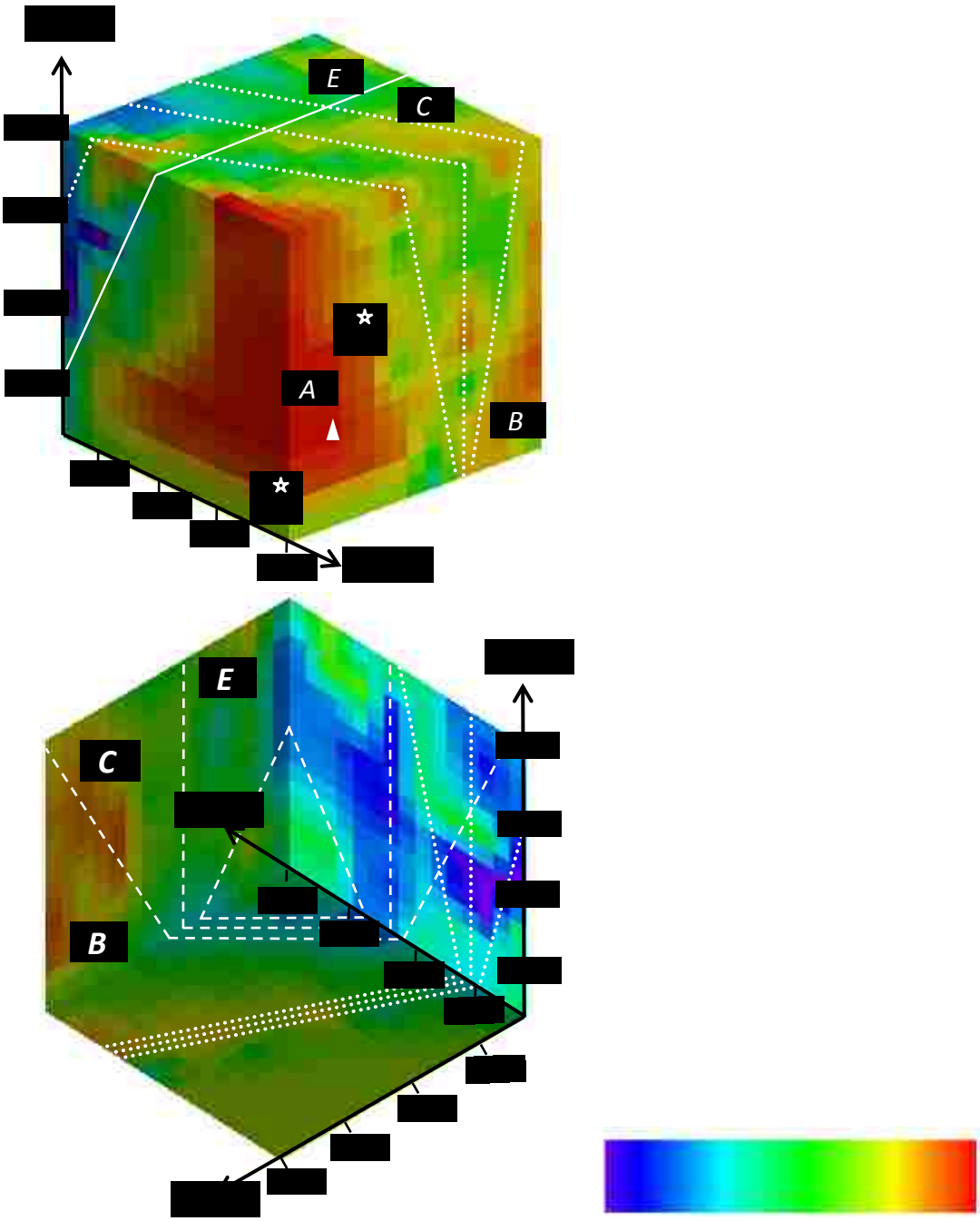

Fig. 4.4 Fidelity of optimized gate CNOT in the $(\Delta_1, \Delta_2, \Delta_{12})$-space. The two different views of the same data cube are given. Red color indicates the fidelity close to 1 (highest); blue color indicates fidelity close to 0.5 (lowest). Low fidelity planes here are indicated by the white lines: solid-plane corresponding to Fig. 2.4 (a); dashed-planes corresponding to Fig. 2.4 (b); dotted-planes corresponding to Fig. 2.4 (c). Letters A, B, C, D and E indicate high fidelity regions. White triangle shows the highest fidelity point. Starts show the sample points which will be discussed in Chapter 5.

highest fidelity point is located at ($\Delta_1, \Delta_2, \Delta_{12}$) = (10, 40, 15) cm^{-1}. It is labeled by white triangle in Fig. 4.4. In vicinity of this point, the fidelity is high, exceeding the value of 0.99.

Δ_1 (cm^{-1})	Δ_2 (cm^{-1})	Δ_{12} (cm^{-1})	Fidelity
5	25	15	0.9903
5	30	15	0.9967
5	35	15	0.9976
5	40	15	0.9970
10	30	15	0.9909
10	35	15	0.9969
10	***40***	***15***	***0.9978***
5	40	20	0.9918
5	40	25	0.9910
5	30	40	0.9958

Table 4.2 High fidelity points in the region A of data cube for gate CNOT (see Fig. 4.4). The highest fidelity point is ($\Delta_1, \Delta_2, \Delta_{12}$) = (10, 40, 15) cm^{-1}.

The transition frequency diagram for this point is shown in Fig. 4.5. On this diagram a set of vertical lines represents the state-to-state transition frequencies in the spectrum of the system. The solid lines in Fig. 4.5 are used for the second (target) mode while the dotted lines are used for the first (control) mode. The vertical axis in Fig. 4.5 shows the value of the dipole moment matrix elements for these transitions. From this diagram, we can see that there is a large separation of frequencies for the transitions in the second mode, and no resonance frequencies for transitions in the first mode.

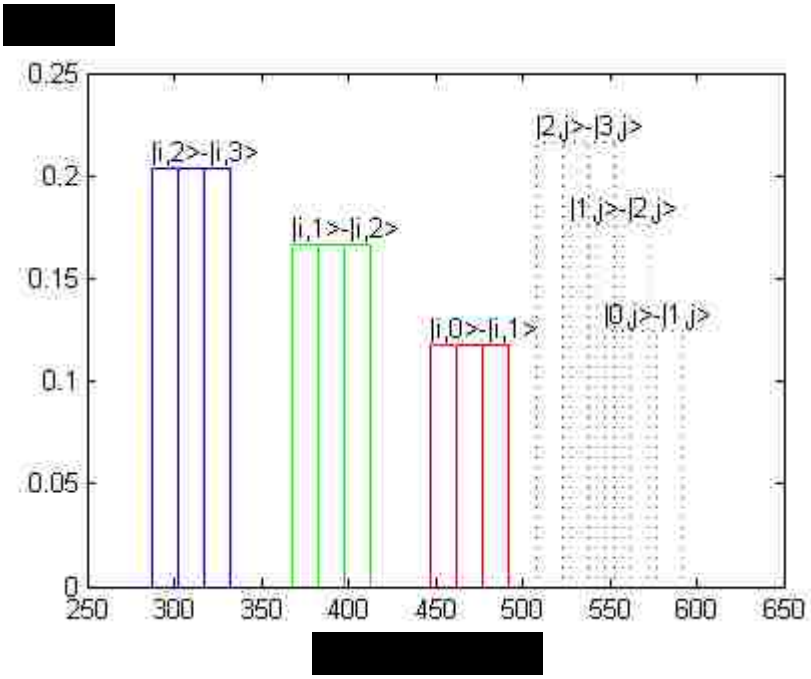

Fig. 4.5 Transition frequency diagram for the two-qubit system described by (Δ_1, Δ_2, Δ_{12}) = (10, 40, 15) cm^{-1} in gate CNOT. None of frequencies are in resonance.

The optimized pulse for this highest fidelity point is shown Fig. 4.6 (a). The time evolution of populations of the qubit states during this pulse is shown in Fig. 4.6 (b-e) for four transitions of Eq. (2.3.1). The optimized pulse has two subpulses. The first subpulse creates an intermediate superposition of the vibrational states in the middle of the pulse and the second subpulse completes the necessary transformation of the qubit state. Four transitions of Figure 4.6 (b-e) exhibit the decrease/increase of the probability during the pulse. The population transfer is basically direct from the initial state to the final state with a negligible population of upper vibrational states.

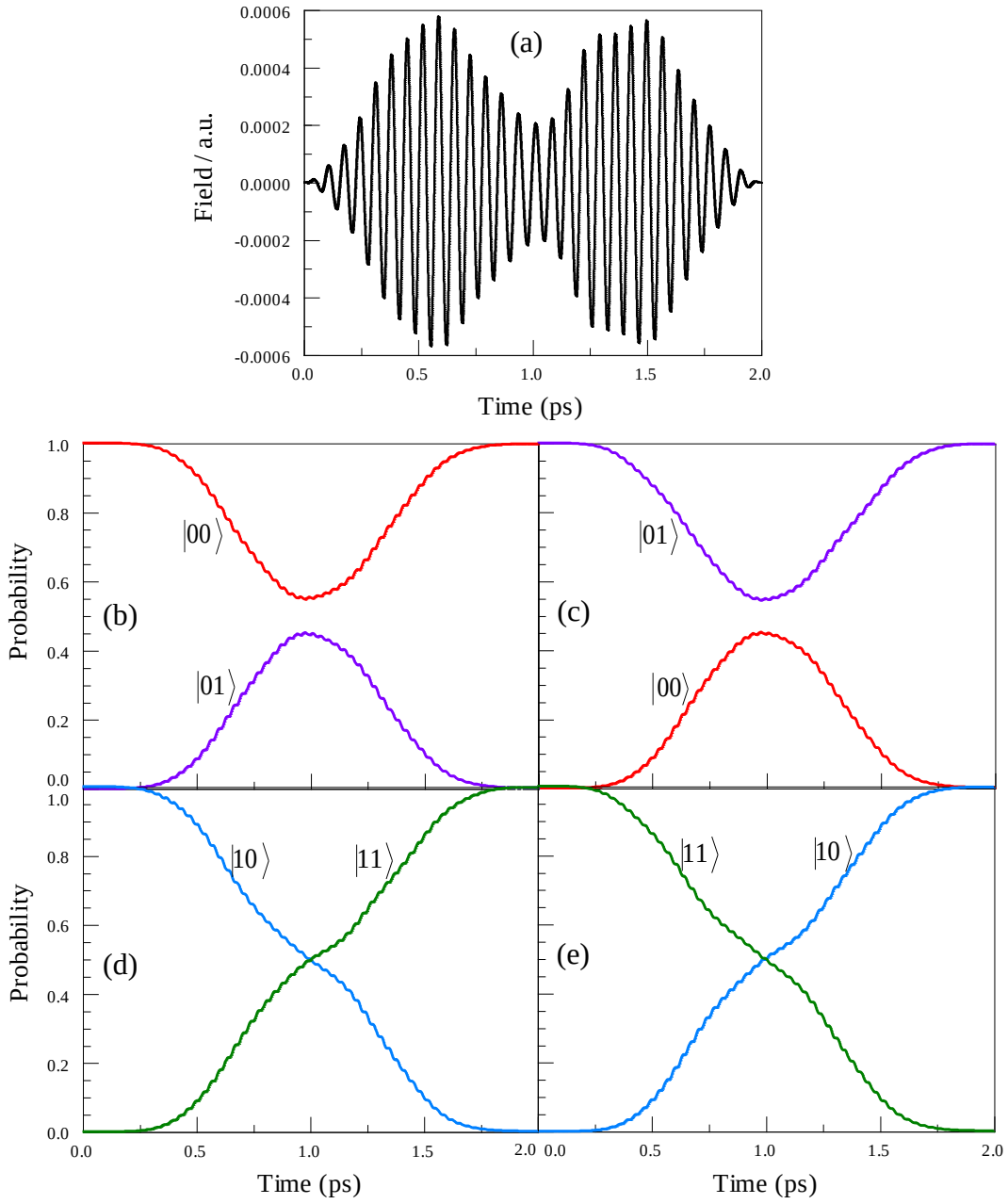

Fig. 4.6 Numerical results for the gate CNOT in the two-qubit system described by $(\Delta_1, \Delta_2, \Delta_{12})$ = (10, 40, 15) cm^{-1}. (a) Optimized 2 ps laser pulse; [(b)-(e)] Evolution of the state populations during the pulse for state-to-state transitions given by Eq. (2.3.1).

(b) Transformation CNOT $|00\rangle \rightarrow |01\rangle$ (c) Transformation CNOT $|01\rangle \rightarrow |00\rangle$

(d) Transformation CNOT $|10\rangle \rightarrow |11\rangle$ (e) Transformation CNOT $|11\rangle \rightarrow |10\rangle$

It is easy to understand why the horizontal plane $b^{(0)}$ affects fidelity of the gate CNOT in the region of small Δ_{12} so badly, having no effect whatsoever on fidelity of the gate NOT (compare Fig. 4.1 and Fig. 4.4). Recall that this plane ($\Delta_{12} = 0$) is due to the pattern of resonances in Fig. 2.2 (c), where the resonant transitions are $|00\rangle \leftrightarrow |01\rangle$ and $|10\rangle \leftrightarrow |11\rangle$. When these two transitions are in resonance and cannot be distinguished one from another, there is simply no way to achieve selectivity and fulfill the requirement of the conditional gate CNOT (i.e., flip the second qubit in the case when the first qubit is in state $|1\rangle$). For the unconditional gate NOT this is not a problem at all because there is no such condition (i.e., state of the second qubit should be flipped in any case). In fact, the optimization task of the unconditional NOT is simplified by the presence of such a resonance. Indeed, since the two transitions are identical, one could simply optimize pulse for one of the two resonant transitions, and then apply it to the other transition with the same high fidelity. This is why the fidelity of unconditional gate NOT is very high in the region with small Δ_{12} (see Fig. 4.1). Note, however, that the plane $b^{(0)}$ is unique in this sense. Inspecting all patterns of resonances in Fig. 2.2 and Fig. 2.3, we concluded that all other low fidelity planes are important for both gates NOT and CNOT.

CHAPTER 5: ANALYSIS AND DISCUSSION

In this Chapter, we take closer look at the effect of the low fidelity planes on the control of the state-to-state transitions. Further insight can be obtained from analysis of evolution of state populations during action of the optimized laser pulse. Here we present such analysis for several sample points in the $(\Delta_1, \Delta_2, \Delta_{12})$-space which we found are typical of a significant number of points in the data cube of Figs. 4.1 and 4.4. These sample points were chosen close to the borders of the high fidelity regions, where we start seeing the negative effects of one or another low fidelity plane (or of several planes simultaneously). For convenience, the sample points are shown as stars in Figs. 4.1 and 4.4.

5.1 Analysis of Gate NOT

The first sample point from the $(\Delta_1, \Delta_2, \Delta_{12})$-space is (40, 25, 5) cm^{-1}, which is at the edge of the high fidelity region B, quite close to the low fidelity planes $c^{(0)}$ and $c^{(+)}$. Fidelity of the optimized gate NOT for this point is not high, just 0.851. The optimized pulse for this point is shown in Fig.5.1 (a). The time evolution of populations of the qubit states during this pulse is shown in Fig. 5.1 (b-e) for four transitions of Eq. (2.2.1). Figure 5.1 (c) shows evolution of state population during the $|01\rangle \rightarrow |00\rangle$ transformation. It is clear from this picture that the low fidelity is due to significant (and unnecessary) excitations of the states $|10\rangle$ and $|11\rangle$ during the pulse.

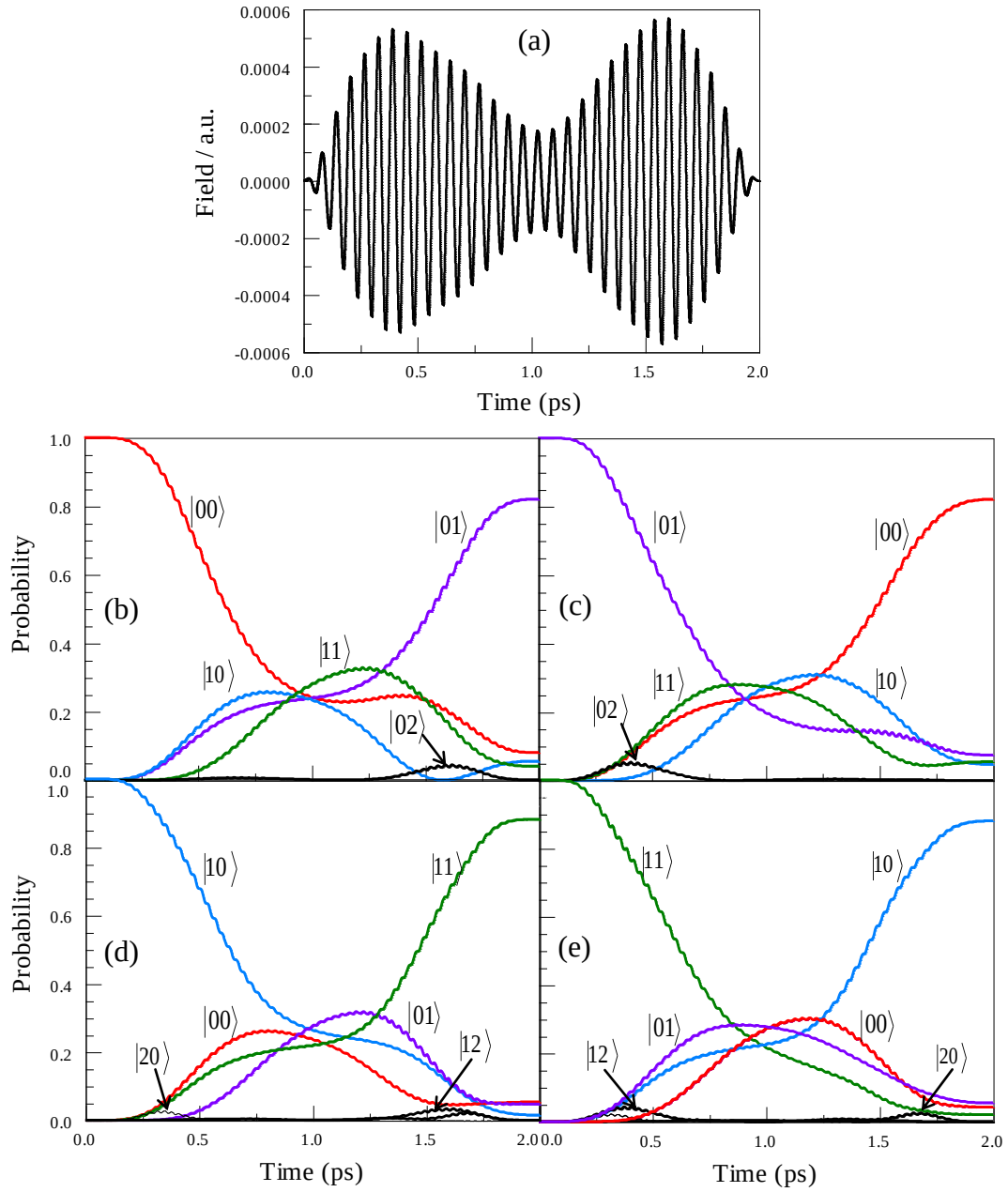

Fig. 5.1 Numerical results for the gate NOT in the two-qubit system described by $(\Delta_1, \Delta_2, \Delta_{12})$ = (40, 25, 5) cm^{-1} (a) Optimized 2 ps laser pulse; [(b)-(e)] Evolution of the state populations during the pulse for state-to-state transitions given by Eq. (2.2.1).

(b) Transformation NOT $|00\rangle \rightarrow |01\rangle$ (c) Transformation NOT $|01\rangle \rightarrow |00\rangle$
(d) Transformation NOT $|10\rangle \rightarrow |11\rangle$ (e) Transformation NOT $|11\rangle \rightarrow |10\rangle$

A non-negligible amount of population remains in these states even at the end of the pulse (which should not happen in the ideal case). Explanation for this result is found in Figs. 2.3 (a) and 2.3 (b), where the resonance patterns for the planes $c^{(0)}$ and $c^{(+)}$ are given. Note that transition $|00\rangle \rightarrow |10\rangle$ in Fig. 2.3 (a) and the transition $|01\rangle \rightarrow |11\rangle$ in Fig. 2.3 (b) are in resonance with the transition $|01\rangle \rightarrow |00\rangle$ we are trying to control, which unavoidably leads to the transfer of population to states $|10\rangle$ and $|11\rangle$. Numerical results of Fig. 5.1 (c) demonstrate that this is exactly what happens.

The second sample point for gate NOT is (30, 30, 5) cm^{-1}, which is at the edge of the high fidelity region B, close to the low fidelity plane $b^{(-)}$. Fidelity of the optimized gate NOT for this point is 0.916. The optimized pulse for this point is shown in Fig.5.2 (a). The time evolution of populations of the qubit states during this pulse is shown in Fig. 5.2 (b-e) for four transitions of Eq. (2.2.1). Figure 5.2 (d) shows evolution of state populations during the NOT $|10\rangle \rightarrow |11\rangle$ transformation. We see that in this example state $|20\rangle$ receives a significant population during the pulse, which is then transferred mostly to the state $|21\rangle$. Some population remains in the state $|21\rangle$ at the end of the pulse, which leads to the reduced fidelity of the gate. Explanation for this effect is found in Fig. 2.3 (f), where the resonance pattern for plane $d^{(-)}$ is given. Note that the transition $|10\rangle \rightarrow |20\rangle$ is in resonance with the transition $|10\rangle \rightarrow |11\rangle$ we are trying to control, which results in transfer of population to the state $|20\rangle$, and finally to the state $|21\rangle$. Numerical results of Fig. 5.2 (d) are in good agreement with

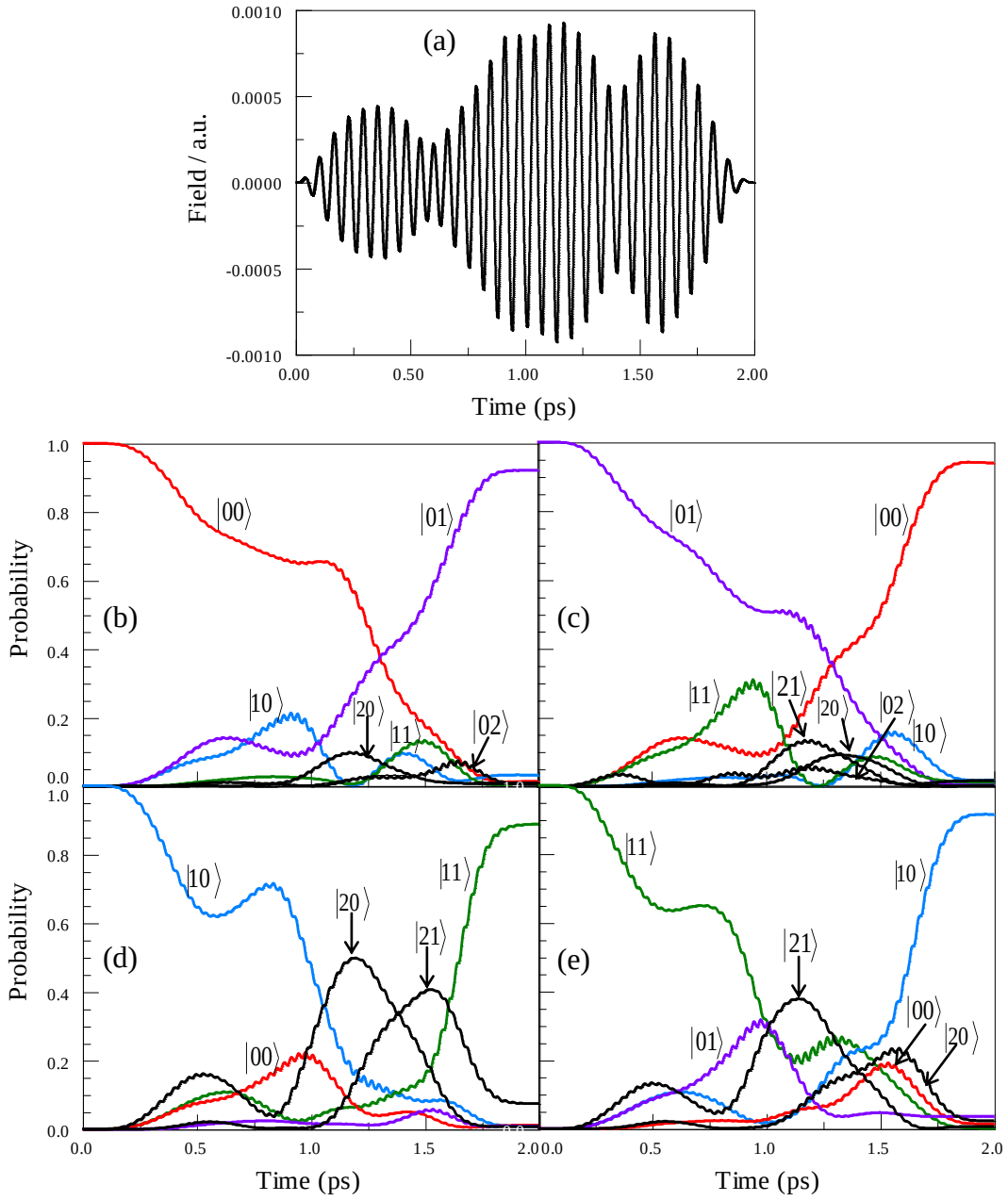

Fig. 5.2 Numerical results for the gate NOT in the two-qubit system described by $(\Delta_1, \Delta_2, \Delta_{12})$ = (30, 30, 5) cm^{-1}. (a) Optimized 2 ps laser pulse; [(b)-(e)] Evolution of the state populations during the pulse for state-to-state transitions given by Eq. (2.2.1).

(b) Transformation NOT $|00\rangle \rightarrow |01\rangle$ (c) Transformation NOT $|01\rangle \rightarrow |00\rangle$

(d) Transformation NOT $|10\rangle \rightarrow |11\rangle$ (e) Transformation NOT $|11\rangle \rightarrow |10\rangle$

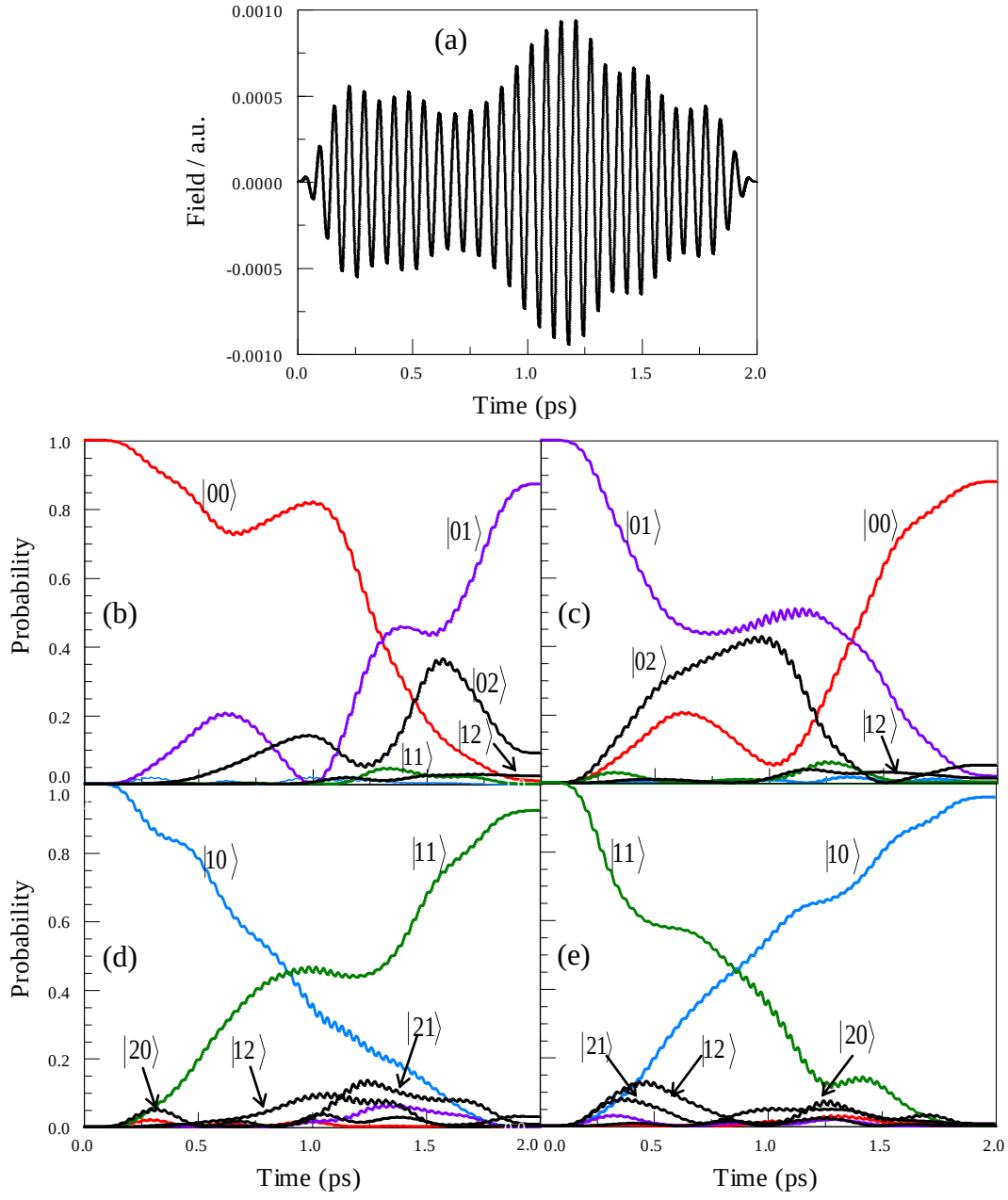

Fig. 5.3 Numerical results for the gate NOT in the two-qubit system described by $(\Delta_1, \Delta_2, \Delta_{12})$ = (5, 20, 20) cm^{-1} shown in Fig. 4.1. (a) Optimized 2 ps laser pulse; [(b)-(e)] Evolution of the state populations during the pulse for state-to-state transitions given by Eq. (2.2.1).

(b) Transformation NOT $|00\rangle \rightarrow |01\rangle$ (c) Transformation NOT $|01\rangle \rightarrow |00\rangle$

(d) Transformation NOT $|10\rangle \rightarrow |11\rangle$ (e) Transformation NOT $|11\rangle \rightarrow |10\rangle$

this explanation. Here, we pause to mention that points in the regions of high fidelity (~0.99) also show some excitation of upper vibrational states during the pulse, but by the end of the pulse all probability is returned back to the qubit states (i.e., controlled) so that the gate fidelity is high.

The last sample point for the gate NOT is (5, 20, 20) cm^{-1}, at the edge of the main fidelity region A, close to the low fidelity plane $a^{(+)}$. Fidelity of the optimized gate NOT for this point is 0.908. The optimized pulse for this point is shown in Fig. 5.3 (a). The time evolution of populations of the qubit states during this pulse is shown in Fig. 5.3 (b-e) for four transitions of Eq. (2.2.1). Figure 5.3 (b) shows evolution of state populations during the $|00\rangle \rightarrow |01\rangle$ transformation. In this case, the low fidelity is mostly due to state $|02\rangle$ which receives significant excitation during the pulse and keeps some residual excitation at the end. Explanation for this effect is found in Fig. 2.2 (d), where the resonance pattern for the plane $a^{(+)}$ is given. Note that the transition $|01\rangle \rightarrow |02\rangle$ is in resonance with transition $|10\rangle \rightarrow |11\rangle$, which we also have to control. Similar to the previous case, this leads to leakage of population from the 2×2 qubit space outside, into the state $|02\rangle$. This process is seen very clearly in the numerical results presented in Fig. 5.3 (b).

5.2 Analysis of Gate CNOT

For the gate CNOT the first sample point we discuss is (5, 40, 10) cm^{-1}, at the lower part of the high fidelity region A, close to the horizontal plane $b^{(0)}$. Fidelity of the optimized gate CNOT for this point is 0.959. The optimized pulse for this point is shown in Fig. 5.4 (a). Time evolution of populations of the qubit states during this

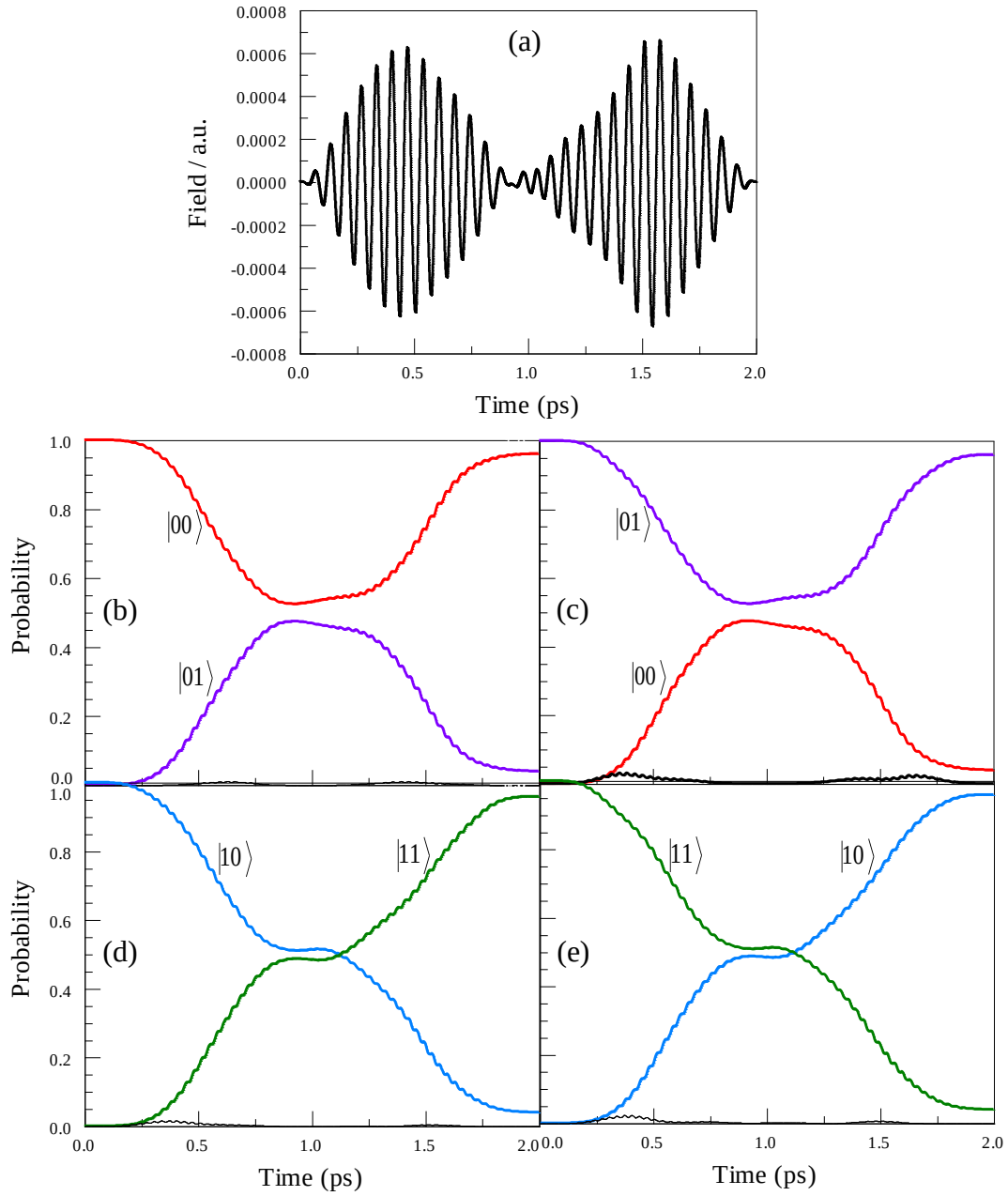

Fig. 5.4 Numerical results for the gate CNOT in the two-qubit system described by $(\Delta_1, \Delta_2, \Delta_{12}) = (5, 40, 10)$ cm^{-1}. (a) Optimized 2 ps laser pulse; [(b)-(e)] Evolution of the state populations during the pulse for state-to-state transitions given by Eq. (2.3.1).

(b) Transformation CNOT $|00\rangle \rightarrow |01\rangle$ (c) Transformation CNOT $|01\rangle \rightarrow |00\rangle$

(d) Transformation CNOT $|10\rangle \rightarrow |11\rangle$ (e) Transformation CNOT $|11\rangle \rightarrow |10\rangle$

pulse is shown in Fig. 5.4 (b-e) for four transitions of Eq. (2.3.1). Figure 5.4 (e) shows evolution of state populations during the CNOT $|11\rangle \rightarrow |10\rangle$ transformation. Here the excitation of upper vibrational states is very low. The fidelity is reduced due to the lack of control of the qubit states: $|00\rangle$, $|01\rangle$, $|10\rangle$ and $|11\rangle$. Explanation for this effect is found in Fig. 2.2 (c), where the resonance pattern for plane $b^{(0)}$ is given. As it was discussed in Chapter 4, transitions $|10\rangle \leftrightarrow |11\rangle$ and $|00\rangle \leftrightarrow |01\rangle$ are in resonance with each other in this case, which causes the equalization of the population between the quit states, and finally to the reduced fidelity. This explanation agrees well with numeric results of Fig. 5.4 (e).

The second sample point for the gate CNOT is (15, 40, 30) cm^{-1}, at the border of the high fidelity region A, close to the plane $d^{(+)}$. Fidelity of the optimized gate CNOT for this point is 0.921. The optimized pulse for this point is shown in Fig.5.5 (a). The time evolution of populations of the qubit states during this pulse is shown in Fig. 5.5 (b-e) for four transitions of Eq. (2.3.1). Figure 5.5 (e) shows evolution of state populations during the CNOT $|11\rangle \rightarrow |10\rangle$ transformation. The low fidelity is due to a cascade of transitions to upper states, up to $|51\rangle$. Explanation for this effect is found in Fig. 2.3 (e), where the resonance pattern for the plane $d^{(+)}$ in is given. We see that in this case the transition $|11\rangle \rightarrow |21\rangle$ is in resonance with one of the transitions we are trying to control ($|00\rangle \rightarrow |01\rangle$), which leads to the leakage of population from the 2×2 qubit space into the state $|21\rangle$, and then to $|31\rangle$, to $|41\rangle$, and even to $|51\rangle$.

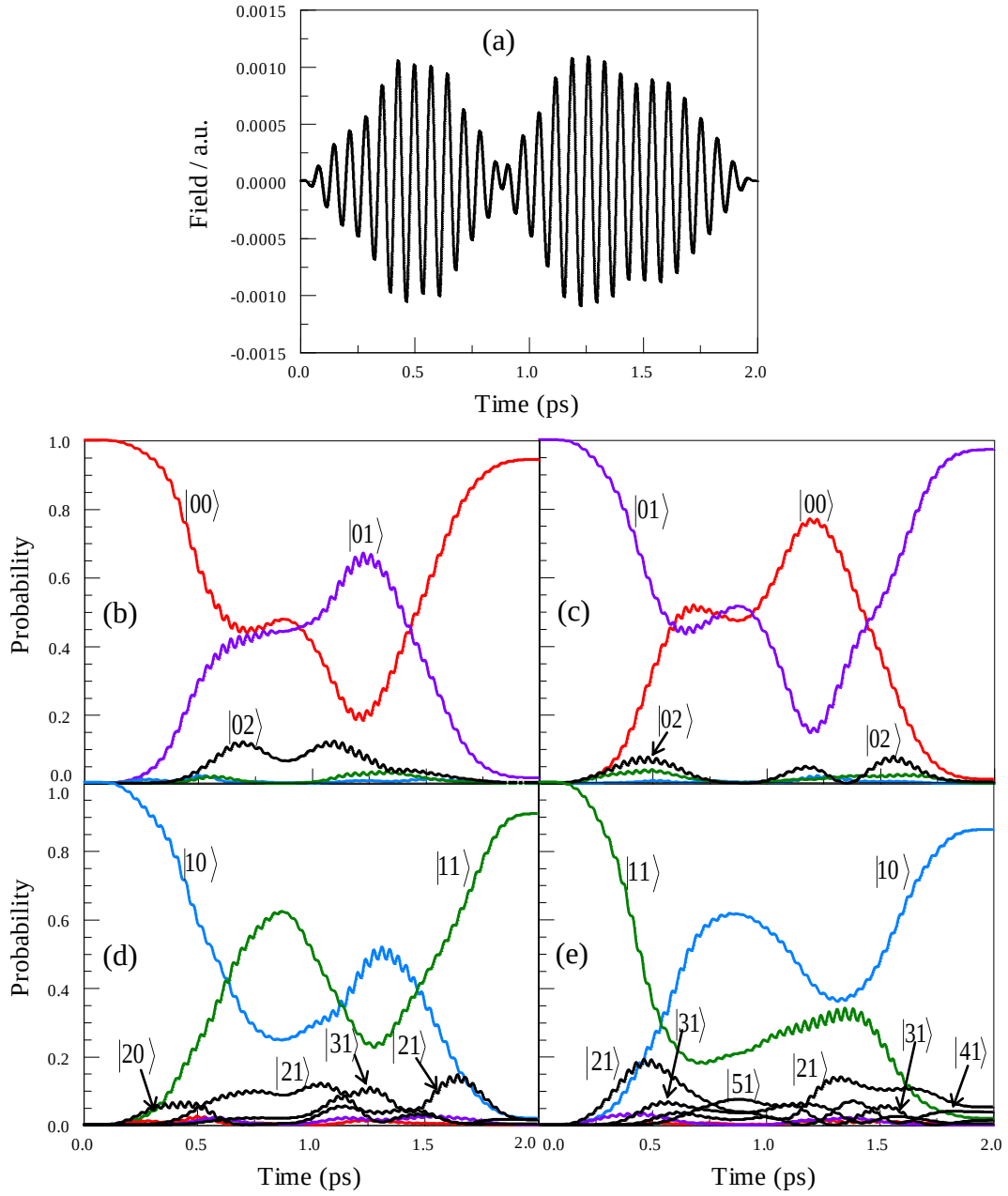

Fig. 5.5 Numerical results for the gate CNOT in the two-qubit system described by $(\Delta_1, \Delta_2, \Delta_{12})$ = (15, 40, 30) cm^{-1}. (a) Optimized 2 ps laser pulse; [(b)-(e)] Evolution of the state populations during the pulse for state-to-state transitions given by Eq. (2.3.1).

(b) Transformation CNOT $|00\rangle \rightarrow |01\rangle$ (c) Transformation CNOT $|01\rangle \rightarrow |00\rangle$

(d) Transformation CNOT $|10\rangle \rightarrow |11\rangle$ (e) Transformation CNOT $|11\rangle \rightarrow |10\rangle$

CHAPTER 6: FORMULATION OF CRITERIA FOR VIBRATIONAL QUBITS

Theoretical analysis in Chapter 2 and numerical results of Chapters 4 and 5 confirm the mechanisms of negative effects of the resonance patterns (Figs. 2.2 and 2.3) on fidelity of gates in the vibrational qubits. The low fidelity of gates can be improved somewhat by other control methods, such as increasing pulse duration[5], searching for optimal pulse duration, or raising intensity of the laser field, but the low fidelity planes will always be there and we believe that a much better way to deal with the control problem is to choose a good candidate molecule, which possesses a suitable set of frequencies and anharmonicities. Such molecule would be represented by a point in the $(\Delta_1, \Delta_2, \Delta_{12})$-space that is far enough from any low fidelity plane. Here we derive a set of simple criteria which should help to evaluate the candidate molecule quickly.

Recall that positions of the four low fidelity planes in Fig. 2.4 (a) do not depend on frequencies of the two-qubit modes (see Eqs. (2.2.3a)−(2.2.3d)). Therefore, these planes are the most general; they will be important with any choice of frequencies and can be avoided only by a proper choice of anharmonicity parameters. Namely, the value of Δ_{12} cannot be arbitrarily small due to the horizontal plane $b^{(0)}$, characterized by $\Delta_{12} = 0$. The choice of sufficiently large Δ_{12} is essential for accurate two-qubit gate CNOT. For example, in our calculations (see Fig. 4.4), the values of $\Delta_{12} > 10\,\text{cm}^{-1}$ resulted in relatively high fidelity (>0.96) for the gate CNOT. So we should require (from Eq. (2.2.3c)):

$$|\Delta_{12}| > \delta, \tag{6.1}$$

where we introduced a tolerance parameter $\delta \sim 10\,\text{cm}^{-1}$ for the thickness of the low fidelity layer in the vicinity the low fidelity plane $\Delta_{12} = 0$. Note further, that there is a relatively little space between planes $a^{(0)}$ and $a^{(+)}$, so that any point in between should be affected either by proximity of the plane $a^{(0)}$ or the plane $a^{(+)}$, or even by both of them simultaneously (see Fig. 2.4 (a)). Numerical results in Figs. 4.1 and 4.4 confirm this observation and demonstrate that, indeed, the fidelity is quite low almost everywhere between planes $a^{(0)}$ and $a^{(+)}$. Thus, it is safer to stay outside of this part of the $(\Delta_1, \Delta_2, \Delta_{12})$-space, which can be achieved by the proper choice of Δ_2. From the Eqs. (2.2.3b) and (2.2.3d), we obtain

$$|\Delta_2| > \tfrac{1}{2}|\Delta_{12}|. \tag{6.2}$$

Here, for simplicity, we did not include the tolerance parameter, but here and everywhere below we will assume that the low fidelity planes exhibit some thickness (so that Eq. (6.2) would have to be written as $|\Delta_2| > \tfrac{1}{2}|\Delta_{12}| + \delta$, for example). The modulus is included in Eq. (6.2) for generality, making it applicable to any quadrant of the $(\Delta_1, \Delta_2, \Delta_{12})$-space. Condition (6.2) seems to be easy to satisfy since in natural molecules the intramode anharmonicities are usually larger than the intermode anharmonicities. It may come as a surprise that the value of Δ_1 is not that important and even $\Delta_1 = 0$ causes no problem by itself. In order to confirm this, we carried out pulse optimization for an additional point (0, 40, 20) outside the data cube and still found a very high fidelity, 0.992.

The value of Δ_1 becomes important if we want to choose a system away from the triplet of the low fidelity planes $d^{(0)}$, $d^{(+)}$ and $d^{(-)}$. These three planes are very close to each other (see Fig.2.4 (c)) and fidelity of gates is low almost everywhere in between (see Figs. 4.1 and 4.4). From Eqs. (2.3.3d), (2.3.3e) and (2.3.3f) we find that one of the two following condition should be satisfied:

$$\Delta_1 < \tfrac{1}{2}\Delta_2 + \tfrac{1}{4}(\omega_1 - \omega_2 - |\Delta_{12}|) \quad , \tag{6.3a}$$

or

$$\Delta_1 > \tfrac{1}{2}\Delta_2 + \tfrac{1}{4}(\omega_1 - \omega_2 + |\Delta_{12}|) . \tag{6.3b}$$

The first of these conditions describes the high fidelity region A in Fig. 4.1, while the region B satisfies the second condition. Since in natural molecules anharmonicities are usually small (compared to frequencies), it seems that satisfying Eq. (6.3a) is easier. So, by choosing the right value of Δ_1 we can avoid the low fidelity layer formed by the triplet of planes $d^{(0)}$, $d^{(+)}$ and $d^{(-)}$ in the $(\Delta_1, \Delta_2, \Delta_{12})$-space. Similar considerations for the triplet of planes $c^{(0)}$, $c^{(+)}$ and $c^{(-)}$ lead to the following criteria:

$$\Delta_1 < \Delta_2 + \tfrac{1}{2}(\omega_1 - \omega_2 - |\Delta_{12}|) \quad , \tag{6.4a}$$

or

$$\Delta_1 > \Delta_2 + \tfrac{1}{2}(\omega_1 - \omega_2 + |\Delta_{12}|) . \tag{6.4b}$$

Again, Eqs. (6.3) and (6.4) also assume some tolerance δ, which is not included explicitly for the simplicity of presentation. Numerical results presented in Figs. 4.1 and 4.4 indicate that in this case $\delta \sim 5$ cm^{-1} is enough.

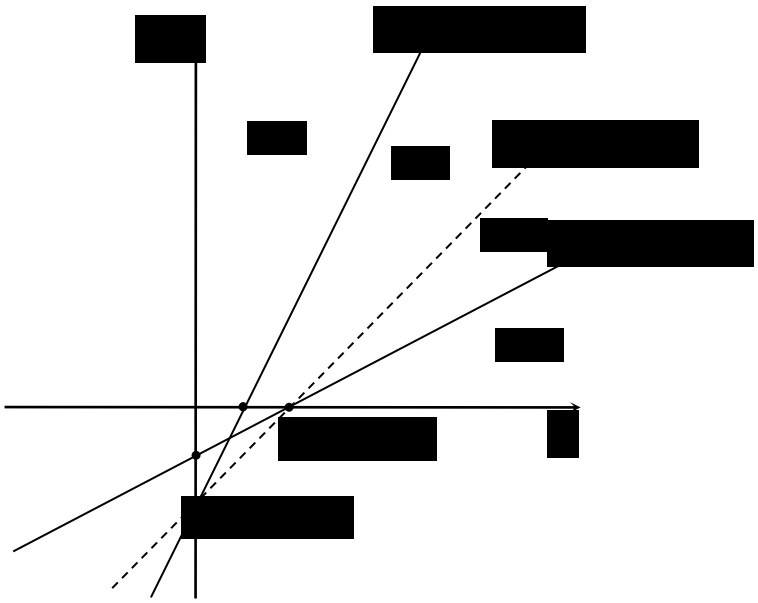

Fig. 6.1 Positions of three triplets of the low fidelity planes as they across the (Δ_1, Δ_2) plane. The triplet planes $c^{(0)}$, $c^{(+)}$ and $c^{(-)}$ in Fig. 2.4 (b) affect both qubits equally. The triplet planes $d^{(0)}$, $d^{(+)}$ and $d^{(-)}$ in Fig. 2.4 (c) affect transformations of the second qubit, while the triplet planes $e^{(0)}$, $e^{(+)}$ and $e^{(-)}$ for Eqs. (6.9) (a, b, c) affect transformations of the first qubit. Letters A and B indicate high fidelity regions when only second (target) qubit is considered (comparing Figs. 4.1 and 4.4). Letters A′ and B′ indicate similar region for the first (control) qubit. Note that the intersection points are defined by the frequency difference.

Another, may be even better solution to eliminate the negative effect of the triplet planes is to choose the values of frequencies such that the entire triplet shifts further away from the origin. Note that vicinity of the origin corresponds to low, naturally occurring and practically interesting values of anharmonicities. Recall that our purpose in Chapters 2, 4 and 5 was to observe and study all the low fidelity planes for methodological purposes; now we will try to suggest how we can avoid seeing the negative effect of these planes. From Eqs. (2.3.3d), (2.3.3e) and (2.3.3f) we see that three planes $d^{(0)}$, $d^{(+)}$ and $d^{(-)}$ cross along the line

$$4\Delta_1 - 2\Delta_2 = \omega_1 - \omega_2$$

in the $\Delta_{12} = 0$ plane, shown in Fig. 6.1. The Δ_1-intercept is $(\omega_1 - \omega_2)/4$. When $\omega_1 = \omega_2$ this line passes exactly through the origin but when the frequency difference is large this line shifts far from the origin. Thus, the condition we need is

$$|\omega_1 - \omega_2|/4 > \delta. \tag{6.5}$$

In the calculations presented in Figs. 4.1 and 4.4 we used $\omega_1 - \omega_2 = 40$ cm^{-1} and this was not quite sufficient to shift the triplet planes $d^{(0)}$, $d^{(+)}$ and $d^{(-)}$ far enough from the origin. It appears that increasing $\omega_1 - \omega_2$ slightly would significantly increase the fidelity of gates in the range of low anharmonicity parameters $\Delta_1 \sim \Delta_2 \sim 10$ cm^{-1}.

Similarly, three planes $c^{(0)}$, $c^{(+)}$ and $c^{(-)}$ cross along the line

$$2\Delta_1 - 2\Delta_2 = \omega_1 - \omega_2$$

in the $\Delta_{12} = 0$ plane (see Fig. 6.1). This line will also shift further away from the origin if the value of $\omega_1 - \omega_2$ larger than 40 cm^{-1} is used. So, choosing appropriate value of $\omega_1 - \omega_2$ (large positive) is a good approach, which shifts both triplets toward the larger values of Δ_1, increasing the overall size of the high fidelity part A and expanding it into the range of small Δ_1 and Δ_2. It is seen from Fig. 6.1 that choosing large negative $\omega_1 - \omega_2$ should also work.

Consider an example: Combining Eqs. (6.1)−(6.5) we can suggest that a very good vibrational two-qubit system can be created by choosing a molecule with the following features:

- $\Delta_{12} > \delta$ (6.6a)
- $\Delta_2 > \Delta_{12}/2$ (Δ_2 as large as possible) (6.6b)

- $\omega_1 - \omega_2 > 4\delta$ ($\omega_1 - \omega_2$ as large as possible) (6.6c)

- $\Delta_1 < \Delta_2 / 2 + (\omega_1 - \omega_2 - \Delta_{12})/4$ (6.6d)

Larger values of Δ_2 and of $\omega_1 - \omega_2$ usually work better and there is no any formal upper limit. Such a system would belong to the high fidelity region A in Figs. 4.1 and 4.4 for the gates NOT and CNOT on the second qubit.

Note, however, that any quantum algorithm requires applying quantum gates to the first qubit as well, which means that the first qubit should also be controlled properly. Thus, several criteria in addition to Eqs. (6.6a)−(6.6d) should be satisfied in order to ensure that the gates on the first qubit are also accurate. We did not do any numerical OCT calculations for the first qubit, but our analytical results can easily be extended onto this case (by permuting indexes "1" and "2" in all equations). First, in order to avoid the effect of a plane similar to $a^{(+)}$, or by analogy with Eq. (6.3b), one needs

- $\Delta_1 > \Delta_{12} / 2$ (6.6e)

A more general condition of this kind, by analogy with Eq. (6.2), can be written as

$$|\Delta_2| > \tfrac{1}{2}|\Delta_{12}|. \quad (6.7)$$

Furthermore, a criterion for the first qubit, analogous to Eq. (6.6d) for the second qubit, should be formulated. But first, let us preclude the derivation with a simple useful example: Imaging a situation when $\Delta_1 \approx \Delta_2$. In this case we do not need an additional criterion for the first qubit and can simply use criterion Eq. (6.6d) of the second qubit, which tells us that if $\Delta_1 \approx \Delta_2$, the values of both anharmonicities

should not approach $(\omega_1 - \omega_2 - \Delta_{12})/2$. Since we do require large positive $\omega_1 - \omega_2$, while the value of Δ_{12} is usually relative small, this condition should be easy to satisfy. In fact, one can neglect Δ_{12} in the criterion Eq. (6.6d), combine Eq. (6.6d) with Eq. (6.6b) and set, as a rule of thumb:

$$\Delta_{12}/2 < \Delta_1 \approx \Delta_2 < (\omega_1 - \omega_2)/2. \qquad (6.8)$$

Here, again, it is understood that Δ_{12} should not be too small (as required for CNOT Fig. 4.4) and some tolerance δ is assumed in each inequality. This simple criterion can be used to quickly evaluate a candidate molecule with $\Delta_1 \approx \Delta_2$ (which may even be desirable for practical reasons not discussed here).

In a general two-qubit case ($\Delta_1 \neq \Delta_2$) one should consider the first qubit explicitly, by writing equations similar to Eqs. (2.3.3a)−(2.3.3f) for two triplets of the low fidelity planes for the first qubit, in exactly the same way as we did it for the second qubit. Or, this can be done easier by interchanging indexes “1” and “2” in all expressions above. We did such transformations. Positions of two triplets of planes for the first qubit are given by equations

$$4\Delta_2 - 2\Delta_1 = -(\omega_1 - \omega_2)$$

and

$$2\Delta_2 - 2\Delta_1 = -(\omega_1 - \omega_2),$$

they are shown in Fig. 6.1 together with positions of triplets for the second qubit. Interestingly, the triplet $c^{(0)}$, $c^{(+)}$ and $c^{(-)}$ for the first and second qubits completely

coincide, which makes the overall picture for two qubits just slightly more complicated than that for the one qubit case (see Fig. 6.1). It also came as a surprise that the overall picture for two qubits is not symmetric with respect to reflection through $\Delta_1 = \Delta_2$ plane. This is simply because the positive values of $\omega_1 - \omega_2$ automatically correspond to negative values of $\omega_2 - \omega_1$ (see Fig. 6.1). The picture is symmetric only when the two qubits are completely identical, i.e., when $\omega_1 - \omega_2 = 0$ and all three lines pass through the origin. It appears, however, that these features simplify the problem, permitting one to shift all four triples of planes (for both qubits) further from the origin by choosing larger value of $\omega_1 - \omega_2$ (positive or negative, see Fig. 6.1).

Unfortunately, the high fidelity region A for the second qubit does not overlap with a similar region of the first qubit (A′ in Fig. 6.1). The high fidelity regions B and B′ do not overlap either (see Fig. 6.1). So, we cannot really formulate a meaningful condition instead of Eq. (6.6d) that would treat the two qubits on equal footing. However we can formulate, in addition to Eq. (6.6d), a condition requiring that the point in A is not too close to the triplet $c^{(0)}$, $c^{(+)}$ and $c^{(-)}$. This is derived by permuting indexes 1 and 2 in Eq. (6.4b), which gives

- $\Delta_1 < \Delta_2 + (\omega_1 - \omega_2 - \Delta_{12})/2$ (6.6f)

Conditions (6.6d) and (6.6f) both cover the high fidelity region A. In the range of small Δ_{12} condition (6.6d) defines the boundary of this region. For larger values of Δ_{12} (and/or) smaller values of $\omega_1 - \omega_2$ condition (6.6f) may become more important as a criterion for the boundary of the region A.

In the criteria (6.6a)−(6.6f) a large positive $\omega_1 - \omega_2$ was assumed for simplicity of presentation and convenience of direct comparison with numerical results of Chapter 4 (Figs. 4.1 and 4.4). However from a general two-qubit perspective, the sign of $\omega_1 - \omega_2$ (and the choice of first and second qubits) does not really matter if $|\omega_1 - \omega_2|$ is so large that all three triplets of planes are very far from origin. In Fig. 6.1 this would correspond to moving all three lines either far to the right (expanding region A onto the entire quadrant) or far to the left (expanding region A′ onto the entire quadrant). If the value of $\omega_1 - \omega_2$ is not that large, which maybe the case in practice, the choice of the first and the second qubits is important. Namely, it is easier to satisfy Eq. (6.3a) if $\omega_1 - \omega_2$ is positive (i.e., $\omega_1 > \omega_2$) and $\Delta_1 < \Delta_2$ at the same time. Note that such set up corresponds to the high fidelity region A in our numerical results (Figs. 4.1 and 4.4). Symmetrically, the assignment $\omega_1 < \omega_2$ with $\Delta_1 > \Delta_2$ is equally good and satisfies Eq. (6.3b). However a system with $\omega_1 > \omega_2$ and $\Delta_1 > \Delta_2$ (or symmetrically with $\omega_1 < \omega_2$ and $\Delta_1 < \Delta_2$) may be hard to control, as it is seen from Eq. (6.3) and Fig. 6.1.

In the discussion above and in the criteria of Eqs. (6.6a)−(6.6f) it is assumed, for simplicity, that all anharmonicities are positive. We did not study the case of the negative anharmoinicities numerically but we believe that the analytical results of Eqs. (6.1)−(6.5), (6.6a)−(6.6f) and (6.10) are general and can be used in any quadrant of the $(\Delta_1, \Delta_2, \Delta_{12})$-space. For example, when both Δ_1 and Δ_2 are negative, the situation is very similar to that discussed above. However, when only one of them is negative, either Δ_1 or Δ_2, the situation is qualitatively different. From Fig. 6.1 it is

very clear that neither triplet of planes passes through the ($\Delta_1 < 0, \Delta_2 > 0$) part of the ($\Delta_1, \Delta_2, \Delta_{12}$)-space. From the previous discussions it is quite clear that a condition for this to be the case is simply $\omega_1 - \omega_2 > 0$, with no restrictions on the values of anharmonicity parameters! Symmetrically, the case of $\omega_1 - \omega_2 < 0$ corresponds to no triplet of planes passing through the ($\Delta_1 > 0, \Delta_2 < 0$) part of the ($\Delta_1, \Delta_2, \Delta_{12}$)-space. This brings us to another important and simple conclusion: Molecule in which one of the modes exhibits negative anharmonicity is a good candidate for quantum computation. There should be another mode with positive anharmonicity and a suitable coupling to the first mode, such that the value of Δ_{12} is not too small (as required for CNOT gate, Eq. (6.1)) and both criteria of Eqs. (6.2) and (6.7) are satisfied. The sign of Δ_{12} does not matter at all (here and in all cases considered above) because pictures of the low fidelity planes (Fig. 2.4) are symmetric with respect to reflection through the $\Delta_{12} = 0$ plane.

Here, for the sake of completeness, we give equations for the triplet of planes for the first qubit (analogous to Eqs. (2.3.3d), (2.3.3e), (2.3.3f)). They can be obtained easily by permuting indexes 1 and 2 in Eqs. (2.3.3d), (2.3.3e), (2.3.3f),

$$2\Delta_1 - 4\Delta_2 = \omega_1 - \omega_2 \tag{6.9a}$$

$$2\Delta_1 - 4\Delta_2 + \Delta_{12} = \omega_1 - \omega_2 \tag{6.9b}$$

$$2\Delta_1 - 4\Delta_2 - \Delta_{12} = \omega_1 - \omega_2 \tag{6.9c}$$

The criteria for avoiding this region of the ($\Delta_1, \Delta_2, \Delta_{12}$)-space (analogous to Eq. (6.4)) can be obtained easily by permuting indexes 1 and 2 in Eqs. (6.4a) and (6.4b),

$$\Delta_1 < 2\Delta_2 + \tfrac{1}{2}(\omega_1 - \omega_2 - |\Delta_{12}|) \tag{6.10a}$$

or

$$\Delta_1 < 2\Delta_2 + \tfrac{1}{2}(\omega_1 - \omega_2 + |\Delta_{12}|) \tag{6.10b}$$

These equations are general so that Eq. (6.10) can be used together with Eqs. (6.1)−(6.5) and (6.7) to evaluate suitability of any point in the $(\Delta_1, \Delta_2, \Delta_{12})$-space for representing a two-qubit system, where the gates on both first and second qubits can be applied with high fidelity. Eqs. (6.6a)−(6.6f) represent a simplified version of Eqs. (6.1)−(6.5), (6.7) and (6.10), adopted for the high fidelity region A. This set of criteria (marked with • symbols) is easier to understand and must be sufficient in most cases. Equation (6.8) is a simple practical criterion for the $\Delta_1 \approx \Delta_2$ case.

CONCLUSIONS:

To conclude, we have obtained a number of general criteria to use for evaluation of candidate molecules for realization of a vibrational two-qubit system. Extension of these ideas onto three and more qubits is relatively straightforward, although simple visualization of such cases is not possible in the 3D space. Our considerations were focused only on major vibrational characteristics (frequencies, anharmonicities and couplings) of the normal mode. The IR intensities of the modes, their couplings to other modes of the molecule, and some other properties may also be important for practical realization but those questions were beyond the scope of this work. For example, it seems that cross terms in the dipole moment function (usually small and neglected here) should permit addressing the degenerate levels differentially from different sets of states, allowing some control at least in principle. We plan to explore this effect theoretically in the future work but we believe that if the control is not impossible, it is still very difficult under highly degenerate conditions. In some real molecules, the vibrational spectrum may differ from the Dunham's expression (2.1.1). We believe that this may lead to transformation of the infinite low fidelity planes into finite regions of space showing some curvature (shells). However, in the vicinity of the origin in the $(\Delta_1, \Delta_2, \Delta_{12})$-space, which is practically important region of weak anharmonicities, those structures must be similar to simple low fidelity planes studied in our work.

BIBLIOGRAPHY

[1] Tesch, C.M.; Kurtz, L.; de Vivie-Riedle, R., *Chem. Phys. Lett.* **2001**, 343, 633.

[2] Tesch, C.M.; de Vivie-Riedle, R., *Phys. Rev. Lett.* **2002**, 89, 158901.

[3] Troppmann, U.; Tesch, C. M.; de Vivie-Riedle, R., *Chem. Phys. Let.*, **2003**, 378, 273.

[4] Tesch, C.M.; de Vivie-Riedle, R., *J. Chem. Phys.*, **2004**, 121, 12158.

[5] Babikov, D., *J. Chem. Phys.* **2004**, 121, 7577.

[6] Bihary, Z.; Clenn, D. R.; Lidar, D. A.; Apkarian, V. A., *Chem. Phys.* **2002**, 360, 459.

[7] Zhu, W.; Botina, J.; Rabitz, J., *J. Chem. Phys.* **1998**, 108, 1953-1963.

[8] Palao, J. P.; Kosloff, R., *Phys. Rev. Lett.* **2002**, 89,188301.

[9] Zadoyan, R.; Kohen, D.; Lidar, D. A.; Apkarian, V. A., *Chem. Phys.* **2001**, 266, 323.

[10] Vala, J.; Amitay, Z.; Zhang, B.; Leone, S. R.; Kosloff, R., *Phys. Rev. A* **2002**, 66, 062316.

[11] Troppmann, U.; de Vivie-Riedle, R., *J. Chem. Phys.* **2005**, 122, 154105.

[12] Zhao, M.; Babikov, D., *J. Chem. Phys.* **2006**, 125, 024105.

[13] Ohtsuki, Y, *Chem. Phys. Lett.* **2005**, 404, 126.

[14] Cheng, T; Brown, A., *J. Chem. Phys.* **2006**, 124, 034111.

[15] Tao, C.; Deselnicu, M.; Mukarakate, C.; Reid, S. A., *J. Chem. Phys.* **2006**, 125, 094305.

[16] Korff, B. M.; Troppmann, U.; Kompa, K. L.; de Vivie-Riedle, R., *J. Chem. Phys.* **2005**, 123, 244509

[17] Zhao, M.; Babikov, D., *J. Chem. Phys.* **2007**, 125, 024105.

[18] Suzuki, S.; Mishima, K.; Yamashita, K., *Chem. Phys. Lett.* **2005**, 410, 358.

[19] Gollub, C.; Troppmann, U.; de Vivie-Riedle, R., *New J. Phys.* **2006**, 8, 48.

[20] Troppmann, U.; Gollub, C.; de Vivie-Riedle, R., *New J. Phys.* **2006**, 8, 100.

[21] Sibert III, E. L.; Gruebele, M.; *J. Chem. Phys.* **2006**, 124, 024317.

[22] Weidinger, D.; Gruebele, M., *Mol, Phys.* **2007**, 105, 1999.

[23] Glenn, D. R.; Lidar, D. A.; Apkarian, V.A., *Mol. Phys.* **2006**, 104, 1249.

[24] Zhao, M.; Babikov, D., *Phys. Rev. A* **2008**, 77, 012338

[25] Ndong, M.; Lauvergnat, D.; Chapuisat, X.; Desouter-Lecomte, M., *J. Chem. Phys.* **2007**, 126, 244505

[26] Shioya, K.; Mishima, K.; Yamashita, K., *Mol. Phys.* **2007**, 105, 1283.

[27] Mishima, K.; Shioya, K.; Yamashita, K., *Chem, Phys. Lett.* **2007**, 442, 58.

[28] Mishima, K.; Tokumo, K.; Yamashita, K., *Chem. Phys.* **2008**, 343, 61.

[29] Weidinger, D.; Gruebele, M., *Chem. Phys.* **2008**, 350,139.

[30] Babikov, D.; Mozhayskiy, V. A.; Krylov, A. I., *J. Chem. Phys.* **2006**, 125, 84306.

[31] Shapiro, E. A.; Spanner, M.; Ivanov, M. Yu., *Phys. Rev. Lett.* **2003**, 91, 237901

[32] Shapiro, E. A.; Walmsley, I. A.; Ivanov, M. Yu., *Phys. Rev, Lett.* **2007**, 98, 050501

[33] Sundermann, K.; de Vivie-Riedle, R., *J. Chem. Phys.* **1999**, 110, 1896.

[34] Sundermann, K.; Rabitz, H.; de Vivie-Riedle, R., *Phys. Rev. A* **2000**, 62, 013409

[35] Shioya, K.; Mishima, K., Yamashita, K., *Mol. Phys*. **2007**, 105, 1283.

[36] Mishima, K., Yamashita, K., *Chem. Phys.* **2010**, 367, 63

[37] Tsubouchi, M., Momose, T., *Phys. Rev. A* **2008**, 77, 052326

[38] Weidinger, D., Gruebele, M., *Chem. Phys.* **2008**, 350, 139

[39] Gu. Y. Y.; Babikov, D., *J. Chem. Phys.* **2009**, 131, 034306.

[40] Sharma, S., Singh, H., Balint-Kurti, G., *J. Chem. Phys.* **2010**, 132, 064108

[41] Tong, X., Winney, A. Willitsch, S., *Phys. Rev. Lett.* **2010**, 105, 143001

[42] Gonzalez-Ferez, R., Mayle, M., Schmelcher, P., *Chem. Phys.* **2006**, 329, 203

[43] Vogelius, I. S., Madsen, L. B., Drewsen, M., *J. Phys. B: At. Mol. Opt. Phys.* **2006**, 39, S1267

APPENDIX A:

Derivation of expression (2.2.3a):

For the pattern of resonances between $|i, j\rangle \leftrightarrow |i, j+1\rangle$ and $|i, j+1\rangle \leftrightarrow |i, j+2\rangle$ transitions, shown in the Fig. 2.2 (a), we can use Eq. (2.1.1) to express corresponding frequencies.

The frequency for transition $|i, j\rangle \leftrightarrow |i, j+1\rangle$ is

$$E_{i,j+1} - E_{i,j} = \omega_2 - \Delta_2(2j+2) - \Delta_{12}(i+\tfrac{1}{2}). \quad \text{(A-1)}$$

where, $E_{i,j} = \omega_1(i+\tfrac{1}{2}) - \Delta_1(i+\tfrac{1}{2})^2 + \omega_2(j+\tfrac{1}{2}) - \Delta_2(j+\tfrac{1}{2})^2 - \Delta_{12}(i+\tfrac{1}{2})(j+\tfrac{1}{2})$

and

$$E_{i,j+1} = \omega_1(i+\tfrac{1}{2}) - \Delta_1(i+\tfrac{1}{2})^2 + \omega_2((j+1)+\tfrac{1}{2}) - \Delta_2((j+1)+\tfrac{1}{2})^2 - \Delta_{12}(i+\tfrac{1}{2})((j+1)+\tfrac{1}{2}) .$$

The frequency for transition $|i, j+1\rangle \leftrightarrow |i, j+2\rangle$ is

$$E_{i,j+2} - E_{i,j+1} = \omega_2 - \Delta_2(2j+4) - \Delta_{12}(i+\tfrac{1}{2}). \quad \text{(A-2)}$$

where,

$$E_{i,j+1} = \omega_1(i+\tfrac{1}{2}) - \Delta_1(i+\tfrac{1}{2})^2 + \omega_2((j+1)+\tfrac{1}{2}) - \Delta_2((j+1)+\tfrac{1}{2})^2 - \Delta_{12}(i+\tfrac{1}{2})((j+1)+\tfrac{1}{2})$$

and

$$E_{i,j+2} = \omega_1(i+\tfrac{1}{2}) - \Delta_1(i+\tfrac{1}{2})^2 + \omega_2((j+2)+\tfrac{1}{2}) - \Delta_2((j+2)+\tfrac{1}{2})^2 - \Delta_{12}(i+\tfrac{1}{2})((j+2)+\tfrac{1}{2}) .$$

So, the final analytic expression for this given resonance patterns of $|i, j\rangle \leftrightarrow |i, j+1\rangle$ and $|i, j+1\rangle \leftrightarrow |i, j+2\rangle$ is to equate the frequencies Eq. (A-1) and Eq. (A-2) as

$E_{i,j+1} - E_{i,j} = E_{i,j+2} - E_{i,j+1}$.

The resultant expression for this given resonance patterns is simply

$\Delta_2 = 0$. (A-3)

Derivation of expression (2.2.3b):

For the pattern of resonances between $|i, j\rangle \leftrightarrow |i, j+1\rangle$ and $|i+1, j+1\rangle \leftrightarrow |i+1, j+2\rangle$ transitions, shown in the Fig. 2.2 (b), we can use Eq. (2.1.1) to express corresponding frequencies.

The frequency for transition $|i+1, j+1\rangle \leftrightarrow |i+1, j+2\rangle$ is

$$E_{i+1,j+2} - E_{i+1,j+1} = \omega_2 (j+1) - \Delta_2 (2j+4) - \Delta_{12} (i+\tfrac{3}{2})(j+1) \quad \text{(A-4)}$$

where,

$$E_{i+1,j+1} = \omega_1 ((i+1)+\tfrac{1}{2}) - \Delta_1 ((i+1)+\tfrac{1}{2})^2 + \omega_2 ((j+1)+\tfrac{1}{2}) - \Delta_2 ((j+1)+\tfrac{1}{2})^2 - \Delta_{12} ((i+1)+\tfrac{1}{2})((j+1)+\tfrac{1}{2})$$

and

$$E_{i+1,j+2} = \omega_1 ((i+1)+\tfrac{1}{2}) - \Delta_1 ((i+1)+\tfrac{1}{2})^2 + \omega_2 ((j+2)+\tfrac{1}{2}) - \Delta_2 ((j+2)+\tfrac{1}{2})^2 - \Delta_{12} ((i+1)+\tfrac{1}{2})((j+2)+\tfrac{1}{2})$$

.

So, the final analytic expression for this given resonances of $|i, j\rangle \leftrightarrow |i, j+1\rangle$ and $|i+1, j+1\rangle \leftrightarrow |i+1, j+2\rangle$ is to equate the frequencies Eq. (A-1) and Eq. (A-4) as

$E_{i,j+1} - E_{i,j} = E_{i+1,j+2} - E_{i+1,j+1}$.

The resultant expression for this given resonance patterns is simply

$$2\Delta_2 + \Delta_{12} = 0. \qquad \text{(A-5)}$$

Derivation for expression (2.2.3c):

For the pattern of resonances between $|i, j\rangle \leftrightarrow |i, j+1\rangle$ and $|i+1, j\rangle \leftrightarrow |i+1, j+1\rangle$ transitions, shown in the Fig. 2.2 (c), we can use Eq. (2.1.1) to express corresponding frequencies.

The frequency for transition $|i+1, j\rangle \leftrightarrow |i+1, j+1\rangle$ is

$$E_{i+1,j+1} - E_{i+1,j} = \omega_2 - \Delta_2(2j+2) - \Delta_{12}(i+\tfrac{3}{2}). \qquad \text{(A-6)}$$

where,

$$E_{i+1,j} = \omega_1((i+1)+\tfrac{1}{2}) - \Delta_1((i+1)+\tfrac{1}{2})^2 + \omega_2(j+\tfrac{1}{2}) - \Delta_2(j+\tfrac{1}{2})^2 - \Delta_{12}((i+1)+\tfrac{1}{2})(j+\tfrac{1}{2})$$

and

$$E_{i+1,j+1} = \omega_1((i+1)+\tfrac{1}{2}) - \Delta_1((i+1)+\tfrac{1}{2})^2 + \omega_2((j+1)+\tfrac{1}{2}) - \Delta_2((j+1)+\tfrac{1}{2})^2 - \Delta_{12}((i+1)+\tfrac{1}{2})((j+1)+\tfrac{1}{2}).$$

So, the final analytic expression for this given resonances of $|i, j\rangle \leftrightarrow |i, j+1\rangle$ and $|i+1, j\rangle \leftrightarrow |i+1, j+1\rangle$ is to equate frequencies Eq. (A-1) and Eq. (A-6) as

$$E_{i,j+1} - E_{i,j} = E_{i+1,j+2} - E_{i+1,j+1}.$$

The resultant expression for this given resonance patterns is simply

$$\Delta_{12} = 0. \qquad \text{(A-7)}$$

Derivation for expression (2.2.3d):

For the pattern of resonances between $|i, j\rangle \leftrightarrow |i, j+1\rangle$ and $|i-1, j+1\rangle \leftrightarrow |i-1, j+2\rangle$ transitions, shown in the Fig. 2.2 (d), we can use Eq. (2.1.1) to express corresponding frequencies.

The frequency for transition $|i-1, j+1\rangle \leftrightarrow |i-1, j+2\rangle$ is

$$E_{i-1,j+2} - E_{i-1,j+1} = \omega_2 - \Delta_2(2j+4) - \Delta_{12}(i-\tfrac{1}{2}) \tag{A-8}$$

where,

$$E_{i-1,j+1} = \omega_1((i-1)+\tfrac{1}{2}) - \Delta_1((i-1)+\tfrac{1}{2})^2 + \omega_2((j+1)+\tfrac{1}{2}) - \Delta_2((j+1)+\tfrac{1}{2})^2 - \Delta_{12}((i-1)+\tfrac{1}{2})((j+1)+\tfrac{1}{2})$$

and

$$E_{i-1,j+2} = \omega_1((i-1)+\tfrac{1}{2}) - \Delta_1((i-1)+\tfrac{1}{2})^2 + \omega_2((j+2)+\tfrac{1}{2}) - \Delta_2((j+2)+\tfrac{1}{2})^2 - \Delta_{12}((i-1)+\tfrac{1}{2})((j+2)+\tfrac{1}{2}).$$

So, the final analytic expression for this given resonances of $|i, j\rangle \leftrightarrow |i, j+1\rangle$ and $|i-1, j+1\rangle \leftrightarrow |i-1, j+2\rangle$ is to equate frequencies Eq. (A-1) and Eq. (A-8) as

$$E_{i,j+1} - E_{i,j} = E_{i-1,j+2} - E_{i-1,j+1}. \tag{A-9}$$

The resultant expression for this given resonance patterns is simply

$$2\Delta_2 - \Delta_{12} = 0. \tag{A-10}$$

APPENDIX B:

Derivation for expression (2.3.3a):

For the pattern of resonances between $|i, j\rangle \leftrightarrow |i, j+1\rangle$ and $|i, j\rangle \leftrightarrow |i+1, j\rangle$ transitions, shown in the Fig. 2.3 (a), we can use Eq. (2.1.1) to express corresponding frequencies.

The frequency for transition $|i, j\rangle \leftrightarrow |i+1, j\rangle$ is

$$E_{i+1,j} - E_{i,j} = \omega_1 - \Delta_1(2i+2) - \Delta_{12}(j+\tfrac{1}{2}) \qquad \text{(B-1)}$$

where,

$$E_{i,j} = \omega_1(i+\tfrac{1}{2}) - \Delta_1(i+\tfrac{1}{2})^2 + \omega_2(j+\tfrac{1}{2}) - \Delta_2(j+\tfrac{1}{2})^2 - \Delta_{12}(i+\tfrac{1}{2})(j+\tfrac{1}{2})$$

and

$$E_{i+1,j} = \omega_1((i+1)+\tfrac{1}{2}) - \Delta_1((i+1)+\tfrac{1}{2})^2 + \omega_2(j+\tfrac{1}{2}) - \Delta_2(j+\tfrac{1}{2})^2 - \Delta_{12}((i+1)+\tfrac{1}{2})(j+\tfrac{1}{2}).$$

So, the final analytic expression for this given resonances $|i, j\rangle \leftrightarrow |i, j+1\rangle$ and $|i, j\rangle \leftrightarrow |i+1, j\rangle$ is to equate frequencies Eq. (A-1) and Eq. (B-1)

$$E_{i,j+1} - E_{i,j} = E_{i+1,j} - E_{i,j}.$$

The resultant expression for this given resonance patterns is simply

$$2\Delta_1 - 2\Delta_2 = \omega_1 - \omega_2. \qquad \text{(B-2)}$$

Derivation for expression (2.3.3b):

For the pattern of resonances between $|i, j\rangle \leftrightarrow |i, j+1\rangle$ and $|i, j+1\rangle \leftrightarrow |i+1, j+1\rangle$ transitions, shown in the Fig. 2.3 (b), we can use Eq. (2.1.1) to express corresponding frequencies.

The frequency for transition $|i, j+1\rangle \leftrightarrow |i+1, j+1\rangle$ is

$$E_{i+1,j+1} - E_{i,j+1} = \omega_1 - \Delta_1(2i+2) - \Delta_{12}(j+\tfrac{3}{2}) \tag{B-3}$$

where,

$$E_{i,j+1} = \omega_1(i+\tfrac{1}{2}) - \Delta_1(i+\tfrac{1}{2})^2 + \omega_2((j+1)+\tfrac{1}{2}) - \Delta_2((j+1)+\tfrac{1}{2})^2 - \Delta_{12}(i+\tfrac{1}{2})((j+1)+\tfrac{1}{2})$$

and

$$E_{i+1,j+1} = \omega_1((i+1)+\tfrac{1}{2}) - \Delta_1((i+1)+\tfrac{1}{2})^2 + \omega_2((j+1)+\tfrac{1}{2}) - \Delta_2((j+1)+\tfrac{1}{2})^2 - \Delta_{12}((i+1)+\tfrac{1}{2})((j+1)+\tfrac{1}{2})$$

.

So, the final analytic expression for this given resonances $|i, j\rangle \leftrightarrow |i, j+1\rangle$ and $|i, j+1\rangle \leftrightarrow |i+1, j+1\rangle$ is to equate frequencies Eq. (A-1) and Eq. (B-3)

$$E_{i,j+1} - E_{i,j} = E_{i+1,j+1} - E_{i,j+1}.$$

The resultant expression for this given resonance patterns is simply

$$2\Delta_1 - 2\Delta_2 + \Delta_{12} = \omega_1 - \omega_2. \tag{B-4}$$

Derivation for expression (2.3.3c):

For the pattern of resonances between $|i+1, j\rangle \leftrightarrow |i+1, j+1\rangle$ and $|i, j\rangle \leftrightarrow |i+1, j\rangle$ transitions, shown in the Fig. 2.3 (c), we can use Eq. (2.1.1) to express corresponding frequencies.

The frequencies for transition $|i+1, j\rangle \leftrightarrow |i+1, j+1\rangle$ is

$$E_{i+1,j+1} - E_{i+1,j} = \omega_2 - \Delta_2(2j+2) - \Delta_{12}(i+\tfrac{3}{2}) \tag{B-5}$$

where,

$$E_{i+1,j} = \omega_1((i+1)+\tfrac{1}{2}) - \Delta_1((i+1)+\tfrac{1}{2})^2 + \omega_2(j+\tfrac{1}{2}) - \Delta_2(j+\tfrac{1}{2})^2 - \Delta_{12}((i+1)+\tfrac{1}{2})(j+\tfrac{1}{2})$$

and

$$E_{i+1,j+1} = \omega_1((i+1)+\tfrac{1}{2}) - \Delta_1((i+1)+\tfrac{1}{2})^2 + \omega_2((j+1)+\tfrac{1}{2}) - \Delta_2((j+1)+\tfrac{1}{2})^2 - \Delta_{12}((i+1)+\tfrac{1}{2})((j+1)+\tfrac{1}{2}).$$

The frequency for transition $|i, j\rangle \leftrightarrow |i+1, j\rangle$ is

$$E_{i+1,j} - E_{i,j} = \omega_1 - \Delta_1(2i+2) - \Delta_{12}(j+\tfrac{1}{2}) \tag{B-6}$$

where,

$$E_{i,j} = \omega_1(i+\tfrac{1}{2}) - \Delta_1(i+\tfrac{1}{2})^2 + \omega_2(j+\tfrac{1}{2}) - \Delta_2(j+\tfrac{1}{2})^2 - \Delta_{12}(i+\tfrac{1}{2})(j+\tfrac{1}{2})$$

and

$$E_{i+1,j} = \omega_1((i+1)+\tfrac{1}{2}) - \Delta_1((i+1)+\tfrac{1}{2})^2 + \omega_2(j+\tfrac{1}{2}) - \Delta_2(j+\tfrac{1}{2})^2 - \Delta_{12}((i+1)+\tfrac{1}{2})(j+\tfrac{1}{2}).$$

So, the final analytic expression for this given $|i+1, j\rangle \leftrightarrow |i+1, j+1\rangle$ and

$|i, j\rangle \leftrightarrow |i+1, j\rangle$ is to equate frequencies Eq. (B-5) and Eq. (B-6) as

$E_{i+1,j+1} - E_{i+1,j} = E_{i+1,j} - E_{i,j}$.

The resultant expression for this given resonance patterns is simply

$$2\Delta_1 - 2\Delta_2 - \Delta_{12} = \omega_1 - \omega_2. \quad \text{(B-7)}$$

Derivation for expression (2.3.3d):

For the pattern of resonances between $|i, j\rangle \leftrightarrow |i, j+1\rangle$ and

$|i+1, j\rangle \leftrightarrow |i+2, j\rangle$ transitions, shown in the Fig. 2.3 (d), we can use Eq. (2.1.1) to express corresponding frequencies.

The frequency for transition $|i+1, j\rangle \leftrightarrow |i+2, j\rangle$ is

$$E_{i+2,j} - E_{i+1,j} = \omega_1 - \Delta_1(2i+4) - \Delta_{12}(j+\tfrac{1}{2}) \quad \text{(B-8)}$$

where,

$$E_{i+1,j} = \omega_1((i+1)+\tfrac{1}{2}) - \Delta_1((i+1)+\tfrac{1}{2})^2 + \omega_2(j+\tfrac{1}{2}) - \Delta_2(j+\tfrac{1}{2})^2 - \Delta_{12}((i+1)+\tfrac{1}{2})(j+\tfrac{1}{2})$$

and

$$E_{i+2,j} = \omega_1((i+2)+\tfrac{1}{2}) - \Delta_1((i+2)+\tfrac{1}{2})^2 + \omega_2(j+\tfrac{1}{2}) - \Delta_2(j+\tfrac{1}{2})^2 - \Delta_{12}((i+2)+\tfrac{1}{2})(j+\tfrac{1}{2})$$

.

So, the final analytic expression for this given $|i, j\rangle \leftrightarrow |i, j+1\rangle$ and

$|i+1, j\rangle \leftrightarrow |i+2, j\rangle$ is to equate frequencies Eq. (A-1) and Eq. (B-8) as

$E_{i,j+1} - E_{i,j} = E_{i+2,j} - E_{i+1,j}$.

The resultant expression for this given resonance patterns is simply

$$4\Delta_1 - 2\Delta_2 = \omega_1 - \omega_2 . \tag{B-9}$$

Derivation for expression (2.3.3e):

For the pattern of resonances between $|i, j\rangle \leftrightarrow |i, j+1\rangle$ and $|i+1, j+1\rangle \leftrightarrow |i+2, j+1\rangle$ transitions, shown in the Fig. 2.3 (e), we can use Eq. (2.1.1) to express corresponding frequencies.

The frequency for transition $|i+1, j+1\rangle \leftrightarrow |i+2, j+1\rangle$ are

$$E_{i+2,j+1} - E_{i+1,j+1} = \omega_1 - \Delta_1(2i+4) - \Delta_{12}(j+\tfrac{3}{2}) \tag{B-10}$$

where,

$$E_{i+1,j+1} = \omega_1((i+1)+\tfrac{1}{2}) - \Delta_1((i+1)+\tfrac{1}{2})^2 + \omega_2((j+1)+\tfrac{1}{2}) - \Delta_2((j+1)+\tfrac{1}{2})^2 - \Delta_{12}((i+1)+\tfrac{1}{2})((j+1)+\tfrac{1}{2})$$

and

$$E_{i+2,j+1} = \omega_1((i+2)+\tfrac{1}{2}) - \Delta_1((i+2)+\tfrac{1}{2})^2 + \omega_2((j+1)+\tfrac{1}{2}) - \Delta_2((j+1)+\tfrac{1}{2})^2 - \Delta_{12}((i+2)+\tfrac{1}{2})((j+1)+\tfrac{1}{2})$$

.

So, the final analytic expression for this given $|i, j\rangle \leftrightarrow |i, j+1\rangle$ and $|i+1, j+1\rangle \leftrightarrow |i+2, j+1\rangle$ is to equate frequencies Eq. (A-1) and Eq. (B-10) as

$$E_{i,j+1} - E_{i,j} = E_{i+2,j+1} - E_{i+1,j+1} .$$

The resultant expression for this given resonance patterns is simply

$$4\Delta_1 - 2\Delta_2 + \Delta_{12} = \omega_1 - \omega_2 . \tag{B-11}$$

Derivation for expression (2.3.3f):

For the pattern of resonances between $|i+1, j\rangle \leftrightarrow |i+1, j+1\rangle$ and $|i+1, j\rangle \leftrightarrow |i+2, j\rangle$ transitions, shown in the Fig. 2.3 (f), we can use Eq. (2.1.1) to express corresponding frequencies.

The final analytic expression for this given $|i+1, j\rangle \leftrightarrow |i+1, j+1\rangle$ and $|i+1, j\rangle \leftrightarrow |i+2, j\rangle$ is to equate frequencies Eq. (B-5) and Eq. (B-8) as

$E_{i+1,j+1} - E_{i+1,j} = E_{i+2,j} - E_{i+1,j}$.

The resultant expression for this given resonance patterns is simply

$$4\Delta_1 - 2\Delta_2 - \Delta_{12} = \omega_1 - \omega_2. \qquad \text{(B-12)}$$

APPENDIX C:

Numerical propagation of the time-dependent Schrödinger equation

$$H\psi = i\hbar\frac{\partial\psi}{\partial t}$$

$$\psi(x,t) = \sum_k C_k(t)e^{-iE_k t}\left|k\right\rangle$$

$$i\dot{\psi} = \left\{-\frac{1}{2m}\frac{\partial^2}{\partial r^2} + V(r) - \mu(r)\varepsilon(t)\right\}\psi$$

$$\dot{C}_k = \frac{d}{dt}C_k$$

$$i\sum_k\left\{\dot{C}_k e^{-iE_k t} + C_k e^{-iE_k t}(-iE_k)\right\}\left|k\right\rangle = \sum_k C_k e^{-iE_k t}\left\{-\frac{1}{2m}\frac{\partial^2}{\partial r^2} + V(r)\right\}\left|k\right\rangle - \sum_k \mu(r)\varepsilon(t)C_k e^{-iE_k t}\left|k\right\rangle$$

$$i\sum_k e^{-iE_k t}\left\{\dot{C}_k + -iE_k C_k\right\}\left|k\right\rangle = \sum_k C_k e^{-iE_k t}E_k\left|k\right\rangle - \sum_k \mu(r)\varepsilon(t)C_k e^{-iE_k t}\left|k\right\rangle$$

$$i\sum_k e^{-iE_k t}\dot{C}_k\left|k\right\rangle + \sum_k e^{-iE_k t}C_k E_k\left|k\right\rangle = \sum_k e^{-iE_k t}C_k E_k\left|k\right\rangle - \sum_k e^{-iE_k t}\mu(r)\varepsilon(t)C_k\left|k\right\rangle$$

$$i\sum_k e^{-iE_k t}\dot{C}_k\left|k\right\rangle = -\varepsilon(t)\sum_k e^{-iE_k t}\mu(r)C_k\left|k\right\rangle$$

Left multiply: $e^{-iE_j t}\left|j\right\rangle$ as $\left\langle j\right|e^{-iE_j t}$

$$i\dot{C}_k = -\varepsilon(t)\sum_k e^{-i(E_k - E_j)t}\mu(r)C_k\left\langle j\right|\mu(r)\left|k\right\rangle$$

$$i\dot{C}_k = -\varepsilon(t)\sum_k e^{-i(E_k - E_j)t}\mu(r)C_k\mu_{jk}$$

$$i\dot{C}_k(t) = -\varepsilon(t)\sum_k e^{-i(E_k - E_j)t}\mu(r)\mu_{jk}C_k(t)$$

$$i(\dot{C}_j^R + i\dot{C}_j^I) = -\varepsilon(t)\sum_k \{\cos[(E_k - E_j)t] - i\sin[(E_k - E_j)t]\}\mu_{jk}(C_k^R + C_k^I)$$

$$\Delta\varphi = (E_k - E_j)t$$

$$i\dot{C}_j^R - \dot{C}_j^I = -\varepsilon(t)\sum_k \{[C_k^R\cos\Delta\varphi + C_k^I\sin\Delta\varphi] + i[C_k^I\cos\Delta\varphi - C_k^R\sin\Delta\varphi]\}\mu_{jk}$$

$$\dot{C}_j^R = -\varepsilon(t)\sum_k [C_k^I\cos\Delta\varphi - C_k^R\sin\Delta\varphi]\mu_{jk}$$

$$\dot{C}_j^I = \varepsilon(t)\sum_k [C_k^R\cos\Delta\varphi - C_k^I\sin\Delta\varphi]\mu_{jk}$$